NREL/TP-214-4591 • UC Category: 271 • DE92001177

NREL/TP--214-4591

DE92 001177

Research on the Structural and Electronic Properties of Defects in Amorphous Silicon

Final Subcontract Report September 1989 - December 1990

R.A. Street
Xerox Palo Alto Research Center
Palo Alto, California

NREL technical monitor: B. Stafford

National Renewable Energy Laboratory
(formerly the Solar Energy Research Institute)
1617 Cole Boulevard
Golden, Colorado 80401-3393
A Division of Midwest Research Institute
Operated for the U.S. Department of Energy
under Contract No. DE-AC02-83CH10093

Prepared under Subcontract No. HB-7-06056-1

December 1991

On September 16, 1991 the Solar Energy Institute was designated a national laboratory, and its name was changed to the National Renewable Energy Laboratory.

Printed in the United States of America
Available from:
National Technical Information Service
U.S. Department of Commerce
5285 Port Royal Road
Springfield, VA 22161

Price: Microfiche A01
Printed Copy A04

Codes are used for pricing all publications. The code is determined by the number of pages in the publication. Information pertaining to the pricing codes can be found in the current issue of the following publications which are generally available in most libraries: *Energy Research Abstracts (ERA)*; *Government Reports Announcements* and Index (*GRA* and I); *Scientific and Technical Abstract Reports (STAR)*; and publication NTIS-PR-360 available from NTIS at the above address.

TABLE OF CONTENTS

LIST OF FIGURES

Fig. 9 Possible structure of a planar platelet formed by H in Si. The edges contain Si-H bonds with strained backbonds. The interior sites are lower energy $(H_2^*)D_n$ sites with binding energies up to 1.0 eV below interstitial H_2 molecules. For very large extended complexes or situations where there are voids or the Si lattice is under significant tension, a (SiHHSi)n configuration plus H_2 molecules in a void becomes comparable in energy to the $(H_2^*)D_n$.

Fig. 10 The solid lines indicate the average energy per H for various configurations versus E_F. The 1H curves represent estimates of the percolation threshold for the various charged states of H obtained by adding 0.5 eV to the lowest stable energy sites for the isolated H.

Fig. 11 Metastability caused by H_2^* dissociation. The H_2^* captures carriers forming unpaired H atoms which diffuse to weak Si-Si bonds (dotted line) forming midgap defects.

Fig. 12 Schematic model for the attachment of silane radicals and hydrogen reactions at the growing surface of a-Si:H.

Fig. 13 The hydrogen density of states distribution showing the modified density of states when the chemical potential is changed.

Fig. 14 Illustration of the range of allowed structural order and hydrogen concentration of a-Si:H and crystalline silicon (c-Si:H). The position marked by the circle corresponds to the surface structure during growth, and the dashed line illustrates the change in structure induced during the subsurface reactions. The H chemical potential is an equivalent measure of order, as described in the text.

Fig. 15 Illustrations of the various hydrogen-induced structural reactions, showing three types of growth, as described in the text.

Fig. 16 Decay of the current after a bias voltage is applied, for voltages from 1 to 12 V. The steady states current at 1V is shown, and the shaded area represents the bulk depletion charge.

Structural and Electronic Properties of Defects in Amorphous Silicon

1. SATURATION OF LIGHT INDUCED DEFECTS

Recent observations find that the light induced defect density saturates at about 10^{17} cm^{-3}. Models relating the defects to the breaking of weak Si-Si bonds do not exhibit an obvious saturation at this density because it is expected that there are many more than 10^{17} cm^{-3} weak bonds. Models which relate the saturation to a small density of special sites such as impurities have similar problems with interpretation. We have studied the light-induced defect density in a-Si:H for a range of illumination intensities and temperatures and have developed a chemical equilibrium model for light induced defect generation, which includes the distribution of weak bonds. A result of the model is that the defect density reaches a saturation value at long illumination time despite the existence of an extended distribution of defect formation sites.

The time dependence of the defect density during soaking was followed by a variation of the CPM method which consists of interrupting the illumination and determining the photon flux ratio r_{CPM}=F(1.15 eV) / F(2.0 eV) which yields the same AC photo-current at the energies of 1.15 eV and 2.0 eV, respectively. The defect density was then taken to be proportional to r_{CPM} . The energy of 1.15 eV was chosen because it lies deep in the region of defect absorption and sufficiently far away from the band tail region. 2 eV photons are completely absorbed by the sample and the the CPM signal is weakly energy dependent in this region. This procedure allows the determination of the defect density in a relatively short time (30 to 40 s). Absolute values for the defect density were obtained by recording full CPM spectra before and after each soaking experiment.

Figure 1 shows the time dependence of the light-induced defect density for different temperatures, for a generation rate $G=4x10^{22}cm^{-3}s^{-1}$. Above room temperature the defect density saturates around ~ $10^{17}cm^{-3}$ for the highest

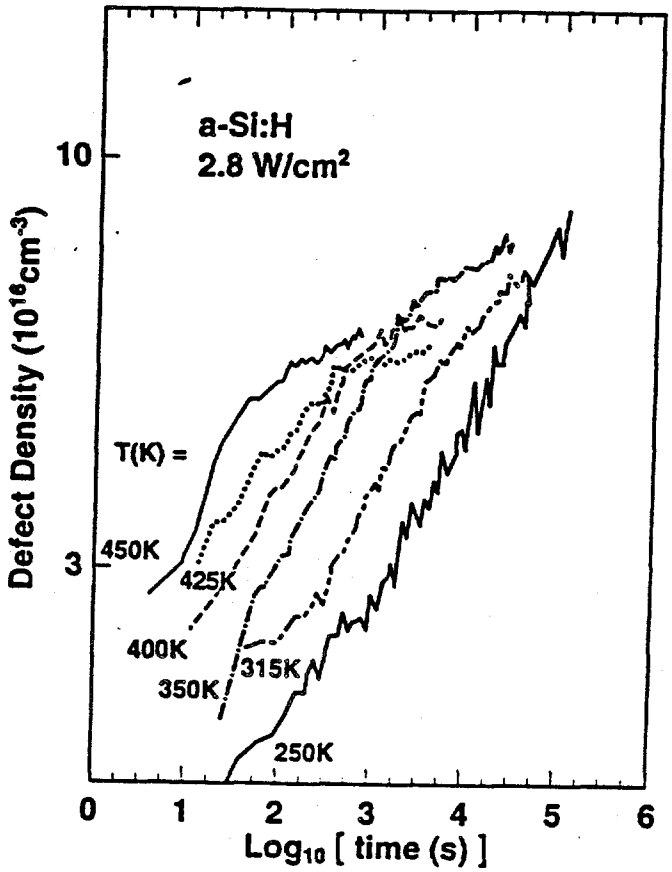

FIG. 1. Time evolution of the light-induced defect density in a-Si:H measured at different temperatures. The sample was irradiated with 2.8 W/cm^2 of monochromatic light (1.92 eV) from a Krypton laser.

illumination intensity used. The saturation values decrease slightly with increasing temperatures. By observing the decay of the defect density after the light is shut off, we verified that the saturation is not due to partial annealing of light-induced defects when the illumination is interrupted to measure the defect density. At room temperature and below, no clear saturation is observed, even after ~ 10^5 seconds of strong illumination. Except for the highest temperatures the curves are approximately parallel in the mid range of defect densities, following a power law time dependence with an exponent η varying from 0.22 to 0.30.

Figure 2 shows the temperature dependence of the defect density in the annealed (dots) and in the light-soaked state (open symbols). Above 390K the dark defect density increases with an activation energy of 0.20 - 0.22 eV due to defect equilibration. The saturated light induced density decreases with increasing temperature, and the effect is stronger for low illumination intensities. Where a clear saturation was not achieved, an arrow was added to the data point to indicate

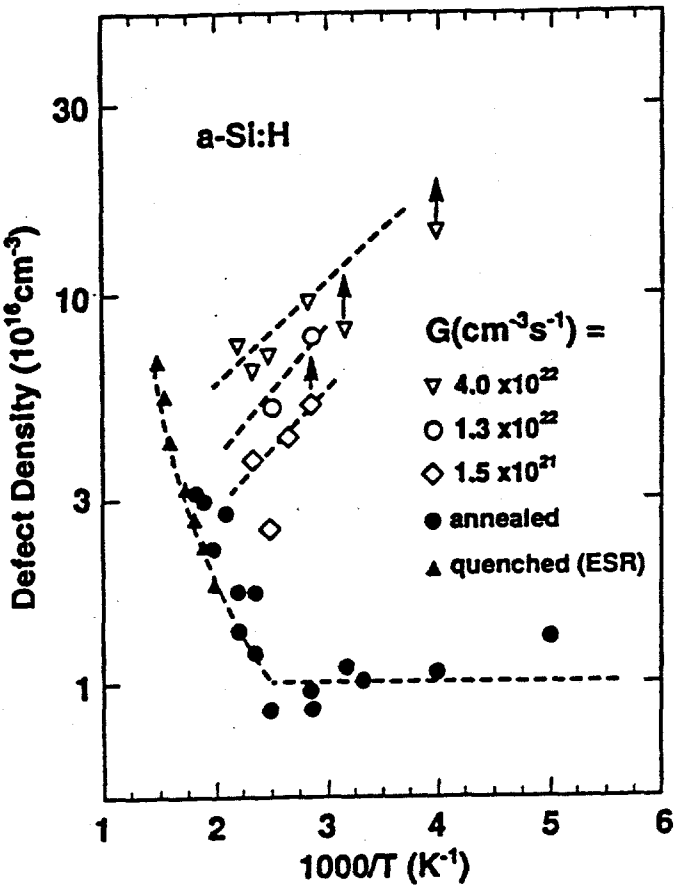

FIG. 2. Temperature dependence of the defect density in the annealed state (solid dots) and after irradiation with 2.8 W/cm^2 (inverted triangles) and 0.065 W/cm^2 (diamonds). The lines represent fits to the model described in the text.

a lower limit for the saturation density. The saturation density depends very weakly on the illumination intensity; an increase in the illumination intensity by a factor of ~ 30 at 400 K leads to a doubling of the saturation density. If a power law dependence of the type $N_{s,\infty} \sim G^{\varepsilon}$ is assumed, the exponent $\varepsilon \sim 0.2$-0.3 at 400 K and decreases at lower temperatures. These results contrast with those reported by Park et al (Appl. Phys. Lett. 59, 493, 1989), who find a room temperature saturation density independent of the generation rate. On the other hand, the intensity dependence we observe is much weaker than predicted by Stutzmann model.

Further indications that saturation depends on light soaking intensity is provided by Fig. 3. The first curve in this figure shows the increase in defect density when the sample was soaked with 580 mW/cm^2 at 350K. The illumination intensity was then decreased by a factor of 10, and the defect density decreases, indicating a reduced saturation level for the weaker illumination. Re-applying the original illumination intensity increases the defect density increases again, as is illustrated in the third

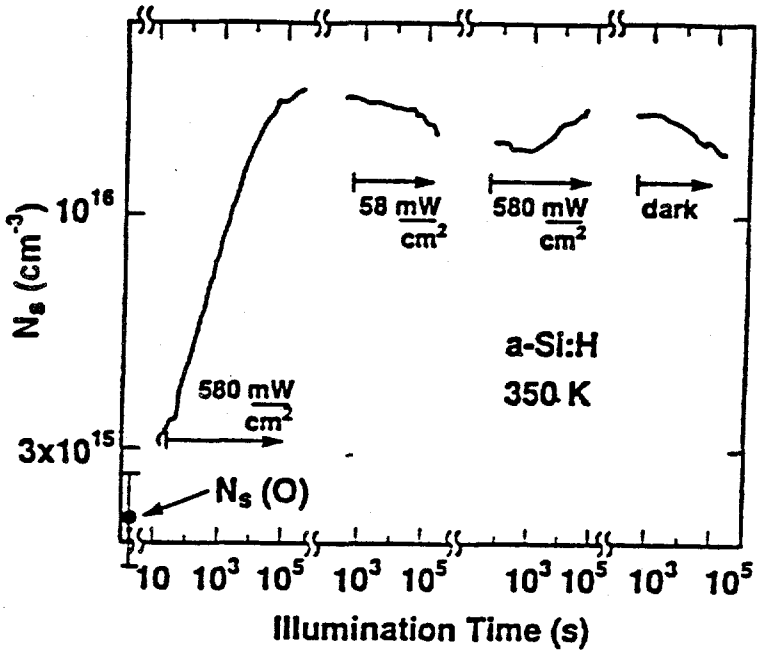

FIG. 3. Time evolution of the defect density for different soaking intensities.

curve. Finally, the last curve displays defect annealing in the dark. Note that neglegible annealing occurs in the time scale of ~ 1 min, when the illumination is interrupted to measure the defect density during soaking.

The dependence of the saturation density N_{sat} on the illumination intensity and on temperature suggests that saturation is due to a balance between defect generation and annealing. Recently, Winer and Street examined thermodynamic models for the equilibrium defect density in undoped a-Si:H based on a chemical equilibrium between weak Si-Si-bonds (SiSi) and neutral dangling bonds (Si-) in the amorphous network. The defect density in the dark is explained by a chemical equilibrium reaction expressed by:

$$SiH + (SiSi) \rightleftharpoons (Si-) + (SiHSi-) \qquad (1)$$

Chemical equilibration at low temperatures takes place through the motion of hydrogen atoms from bond terminating sites (SiH) to a weak-bond sites (SiSi) that make the valence-band tail of localized states, leading to the formation of two defects. A strict thermodynamic analysis of the chemical reactions cannot be made under illumination, since the material is not in equilibrium. In order to extend the chemical equilibrium model to calculate the steady-state defect density under illumination, we assume that the sole effect of illumination is to shift the electron and hole quasi-Fermi levels, E_{Fn} and E_{Fp}, towards the conduction and valence bands.

The defect formation energy is reduced when an electron-hole pair is involved in the defect formation reaction, so that more defects are thermally generated at a given temperature.

Different defect formation reactions involving photo-generated carriers are possible, but we only consider here the simple process involving an electron-hole pair (e-h) described by the reaction:

$$SiH + (SiSi) + e + h \rightleftharpoons (Si\text{-}) + (SiHSi\text{-}) \qquad (2)$$

The enthalpy change for this reaction is smaller than that for Eq. 1 by the energy difference E_{Fn}-E_{Fp} between the electron and hole quasi-Fermi levels. The defect chemical potential under illumination μ is,

$$\mu = 2E_D - (E_{Fn} - E_{Fp}) + (kT/2)\ln(N_D/N_H) \qquad (3)$$

μ depends on the quasi-Fermi levels and therefore on the generation rate G . With increasing illumination levels, μ moves closer to the valence band edge, and more weak bonds are transformed into defects. The defect creation process is self-limiting since the newly created recombination centers reduce E_{Fn} and E_{Fp} , inhibiting further defect formation

In order to obtain the defect chemical potential from Eq. 4 it is necessary to relate the quasi-Fermi levels E_{Fn} and E_{Fp} to the defect density and to the carrier generation rates G . We assume the following simple approximation for E_{Fn} :

$$E_c - E_{Fn} \simeq -kT\,ln\left(\frac{G^{\gamma_n}}{A_n N_c N_s} + e^{-E_a/kT}\right) \qquad (4)$$

with $\gamma_n \sim 1$. Here, E_C is the mobility gap, N_c is the effective density of states at the mobility edge, N_s is the defect density, E_a is the activation energy for the dark conductivity, and A_n is the electron capture probability of the recombination centers. A similar expression was used to calculate the hole quasi-Fermi level.

Evaluation of the equilibrium condition of reaction 2 yields the following analytical approximation for the saturation defect density N_{sat} in the low temperature range ($T << T_v$):

$$N_s^{\infty} \approx 2\left[k\left(\frac{2T_v^2}{2T_v - T}\right)N_{v0}\right]^{2/\zeta} exp\left[-\frac{2E_D - E_c}{\zeta k T_v}\right]\left(\frac{N_H G^{(\gamma_n + \gamma_p)}}{A}\right)^{\beta/\zeta} \qquad (5)$$

with $\beta = T/T_v$, $A \simeq 4A_n N_c A_p N_v$, and $\zeta \simeq 2+3\beta$

Equation 6 predicts a power-law dependence of the saturation defect density on the generation rate G with a temperature dependent exponent,

$$\varepsilon = (\gamma_n + \gamma_p)\beta/[2+3\beta]. \qquad (6)$$

Assuming a characteristic tail temperature $T_v = 550K$, and $\gamma_{n,p} = 1$, we obtain an exponent ε that varies between $\varepsilon = 0.27$ at 250K and $\varepsilon = 0.35$ at 400K, which agrees with the experimental value in this temperature range. Lower values of ε are obtained if the $\gamma_{n,p}$ are smaller.

In order to test the chemical equilibrium model described by Eq. 5, the steady-state defect density under illumination was calculated for the experimental conditions of Fig. 2. The results are the lines superposed on the experimental points in Fig. 2. We restrict ourselves again to the simple case where $\gamma_{n,p} = 1$ and we considered the equilibrium Fermi-level to coincide with the defect level E_D, i.e., $E_a = E_c - E_D$. Finally, in order to shift the curves vertically and obtain better agreement with the experimental data, we scaled the capture probabilities A_n and A_p by a constant factor $k_s = 2.5 \times 10^4$.

The solid line in Fig. 2 is the calculated equilibrium defect density in the dark which reproduces the experimental data. The defect density under illumination was calculated for carrier generation rates of $4 \times 10^{22} cm^{-3}$ (upper curve) and $1.5 \times 10^{21} cm^{-3}$ (lower curve). The model predicts that the saturation defect density decreases in the low temperature region, with an effective activation energy of 0.10 - 0.15 eV. The model gives a reasonable agreement to the experimental data in the high temperature region. Unfortunately, precise comparison between these two models and experimental data in the low temperature region is difficult since a clear saturation in the density of light-induced defect in not reached even after long illumination times (see Fig. 1). This is indicated by the arrows on the experimental points in Fig. 2, which in this case correspond to a lower limit for the saturation density.

2. HYDROGEN MEDIATED METASTABILITY AND GROWTH.

There is strong circumstantial evidence for the role of hydrogen in the metastability, although a complete proof is still lacking. The evidence stems primarily from the observations of hydrogen motion at the same temperature as the metastability effects. The activation energy of defect annealing is comparable with

that of hydrogen diffusion. Furthermore, the doping trends are the same - dopants which result in a larger hydrogen diffusion coefficient also lead to faster defect relaxation. In addition, the stretched exponential form of the relaxation is in quantitative agreement with the dispersive time dependence of the hydrogen diffusion. Finally, the observation of hydrogen diffusion implies that the hydrogen distribution is in equilibrium, and therefore that any defect associated with the breaking of a Si-H bond are also in equilibrium. Thus the defect equilibration is a predicted consequence of the hydrogen diffusion.

The relation between hydrogen and the structure of a-Si:H has been explored from various directions. The following sections consider the hydrogen bonding distribution, chemical reactions and energetics, and apply these results to models for metastability and growth of films.

A. Hydrogen chemical reactions

Light-induced defects are one of a broad class of metastable defect creation processes. Other examples include defects induced by quenching from high temperature, charge accumulation at interfaces, doping, electric current, etc. Metastability results from a thermally activated recovery, such that the relaxation rate,

$$\tau_R = \omega_o^{-1} \exp(E/kT) \qquad (7)$$

is very long at room temperature. Thus, the defects remain when the creation source is removed, but are annihilated by annealing at elevated temperatures (typically 100-200°C). Fig. 4 summarizes defect creation and annihilation processes which can be by internal thermal excitation, or by an external excitation such as recombination, trapping or a shift of the Fermi energy.

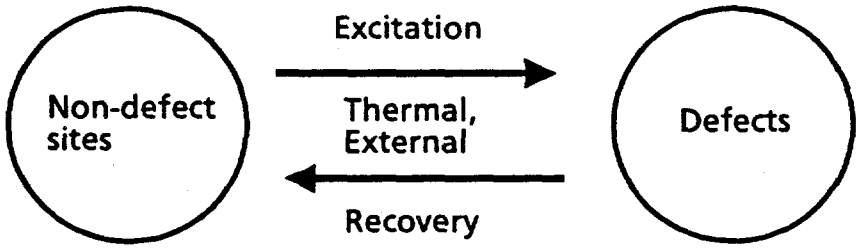

FIGURE 4. Illustration of the reversible transfer between non-defect and defect sites by different excitation mechanisms.

The reversible metastable effects may be grouped according to their type as follows.

Non-equilibrium effects. These occur when there is a non-thermal source of energy to create defects, such as trapping or recombination of electrons and holes. There is a low thermal activation energy for defect creation because part of the energy arises from the recombination. Examples are light-induced defects and current-induced defects.

Equilibrium effects. Defects are created thermally in an equilibrium process. Examples are thermally- and bias-induced defects, and defects in doped a-Si:H. There is a high activation energy (~1 eV) for creation and annealing, and both rates have stretched exponential kinetics. Quenching from high temperature freezes in a high defect density, which is reduced by annealing at a lower temperature. A shift of the Fermi energy associated with charge accumulation at an interface or doping, reduced the defect formation energy and creates defects. Dopants also have metastable properties and a temperature dependent doping efficiency.

The proposal that hydrogen controls the metastability effects assumes that defects are created by hydogen migration between alternative bonding sites, specifically Si-H and Si-Si bonds. The reaction,

$$\text{Si-H} + \text{Si-Si} \leftrightarrows \text{Si}\bullet + \text{Si-H}\bullet\text{Si} \qquad (8)$$

corresponds to the transfer of one hydrogen and the creation of two defects, both of which are dangling bonds (denoted Si•) but in different local environments. A second reaction,

$$\text{Si-H} + \text{Si-H}\bullet\text{Si} \leftrightarrows \text{Si}\bullet + \text{Si-HH-Si} \qquad (9)$$

results in both defects at Si-H sites and the Si-Si bond broken but fully passivated by the two hydrogen atoms. The energy to insert hydrogen into a Si-Si bond is quite large and is accompanied by a significant relaxation of the silicon atoms. The energy is reduced if the bond is suitably distorted, leading to the idea of preferential hydrogen insertion into weak bonds. Reaction 9, when applied to a distribution of weak bonds is one manifestation of the weak bond-dangling bond conversion model and calculations find that it agrees well with the observed equilibrium defect density in undoped a-Si:H (Street and Winer, Phys. Rev. B40, 6236, 1989).

Reaction 10 shows how an Si-Si bond can satisfy its bonding requirements by incorporating two H atoms. The combined reaction,

$$2\,\text{Si-H}\bullet\text{Si} \leftrightarrows \text{Si-Si} + \text{Si-HH-Si} \qquad (10)$$

may be exothermic, because the configurations on the right side are low energy states containing no unsatisfied bonds, provided that the network is sufficiently flexible to incorporate the two hydrogen atoms. This confers the Si-Si bond with the property of a negative hydrogen correlation energy (negative U_H), analogous with negative U electronic defects sometimes found in the presence of a large lattice relaxation.

B. Hydrogen density of states model and metastability

Chemical reactions become inconvenient when the energy states are broadened by disorder. We propose that the hydrogen density of states (HDOS) is a useful representation of the chemical reactions, and is illustrated in Fig. 5a. The vertical

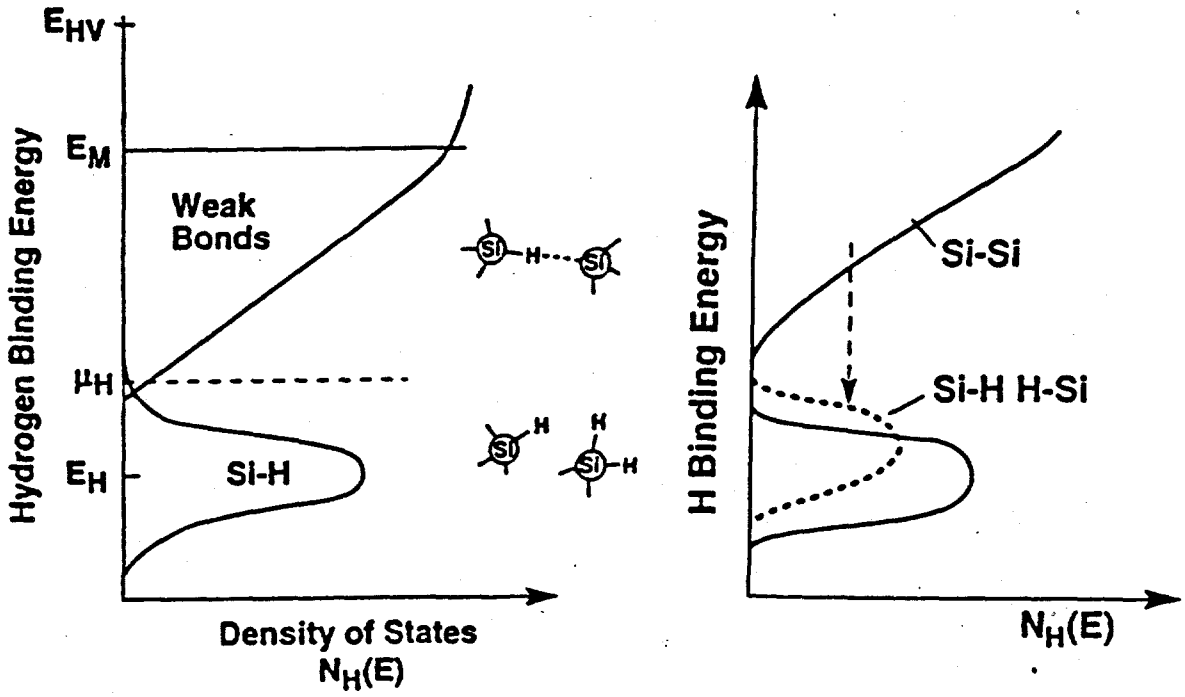

Fig. 5. (a) Illustration of the HDOS distribution showing the Si-H bonding states centered at energy E_H, the migration energy E_M, the chemical potential, μ_H and the energy E_{HV} of hydrogen in vacuum. (b) Illustration of the HDOS for two-hydrogen states with large structural relaxation.

axis is the energy of hydrogen in the various configurations, and the horizontal axis is the number $N_H(E)$ of states at energy E. Fig. 5a shows Si-H states which are occupied by hydrogen, apart from the small density of Si dangling bonds, and the Si-Si bonds which are empty of hydrogen except for the few defects of the Si-H •Si

type. The HDOS is referenced to the energy E_{HV} of atomic hydrogen in a vacuum, and the energy of hydrogen migration at E_M is estimated to be 0.5-1 eV below E_{HV}. Negative U_H states can be included in the HDOS, as illustrated in Fig 5b, and consist of a band of Si-HH-Si below the singly occupied weak bond states.

The equilibrium hydrogen distribution is described by a chemical potential μ_H which separates the occupied and unoccupied states. The hydrogen diffusion and the defect density are both given in terms of μ_H and $N_H(E)$. The defect density is minimized when μ_H lies in the minimum $N_H(E)$ between the Si-H bonds and the Si-Si bonds. It seems plausible that chemical reactions during growth cause μ_H to be positioned such that the defect density is minimized.

The HDOS approach leads to a new description of metastability which focusses attention on the hydrogen distribution. The equilibrium defect density is given by the Fermi distribution of hydrogen and is the sum of the unoccupied Si-H states and the singly occupied weak bonds. Non-equilibrium metastability follows from the excitation of hydogen into a non-equilibrium distribution, as is illustrated in Fig. 6. The recombination of an electron-hole pair is assumed to excite hydrogen off a Si-H bond into the distribution of weak bonds. Deep trapping of the hydrogen at the weak bonds corresponds to metastable defect creation, and annealing allows the hydrogen to migrate and return to its original distribution. These processes are analogous to electronic photoconductivity and trapping of carriers in deep states. Thus we anticipate describing the process in terms of excitation, trapping and recombination steps, but of hydrogen atoms instead of electronic carriers.

Excitation. There is good evidence that defect creation results from the energy released by the recombination of an electron-hole pair or the trapping of a single carrier, but the details of the mechanism are not yet completely clear. A phonon mechanism is usually assumed in which the recombination energy is transferred to vibrational excitations. Here it is assumed that the energy excites hydrogen from an Si-H bond to a weak bond state. Additional thermal excitation may be needed if the recombination energy is insufficient to break the bond and the additional thermal energy should be observed in the activation energy of the excitation rate. Light-induced defect creation has a low activation energy, indicating that the recombination energy is almost sufficient to release hydrogen, as might be expected since the hydrogen diffusion energy (1.5 eV) is less than the band gap energy.

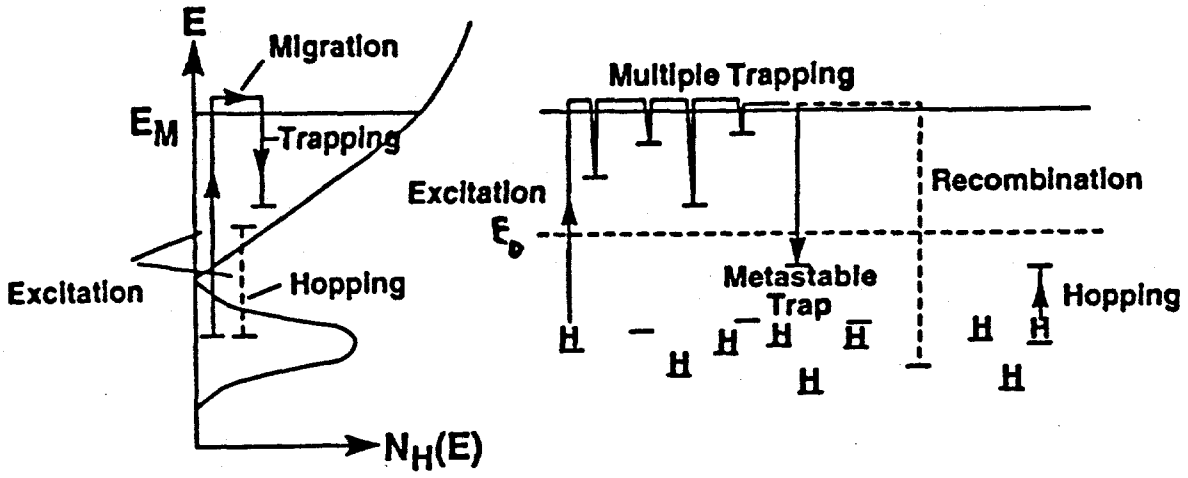

Fig. 6. Illustration of possible hydrogen excitation, trapping and recombination mechanisms leading to light-induced defect creation, as described in the text.

Defect creation by trapping of a single carrier releases a smaller energy and is expected to have a larger activation energy.

Hydrogen trapping and defect formation. The excited hydrogen must reach a trapping site of high binding energy to form a metastable defect. Figure 6 shows two possible mechanisms of hydrogen trapping. The hydrogen is free to migrate away if it is excited into the mobile state at E_M, provided that immediate recombination does not occur. We anticipate that the subsequent migration follows a multiple trapping mechanism within the distribution of weak bonds, until it reaches a trap which is sufficiently deep that it is not released within the time scale, t, of the experiment. A demarcation energy, E_D, can be defined, as in the multiple trapping model of electronic carriers,

$$E_D = E_M - kT \ln(\omega_o t) \qquad (11)$$

E_D defines the minimum trap depth for which release does not occur within time t. E_D is about E_M-1 eV at room temperature and a time of 10^3-10^4 sec.

The multiple trapping model suggests that hydrogen migrates a substantial distance before finding a metastable site. Assuming an exponential tail to the distribution of weak bonds of slope E_o=0.1 eV, then the fraction of states further from E_M than E_D is $f \sim \exp(-E_D/E_o)$. The average number of migration steps is 1/f for which the diffusion distance, R_D, is

$$R_D = af^{-1/2} = a \exp(E_D/2E_o) \sim 500\text{Å} \qquad (12)$$

where a is the mean free path for hydrogen capture, taken to be 3Å.

An alternative trapping mechanism applies when hydrogen makes a direct hop to a weak bond site, as illustrated in Fig. 6. The Si-H bond is assumed to be immediately adjacent to the trapping site; an example is the model proposed by Stutzmann, Jackson and Tsai, in which a hydrogen atom remains attached to the same Si atom, but rotates into a weak bond. This type of mechanism has the advantage of probably requiring a lower excitation energy (although there must be a barrier to prevent immediate recombination), but presumably can only occur at a small fraction of all the sites.

Recombination. The analogy between this metastability model and electronic photoconductivity leads us to expect that a steady state defect density is eventually reached when excitation and recombination rates balance. It is not necessary that all the available defect sites are occupied, and indeed the occupancy fraction might be very low. Recombination is illustrated in Fig. 6, and occurs when the migrating hydrogen binds to a dangling bond. The steady state concentration of defects depends on the relative capture cross-sections for trapping at dangling bonds and weak bonds, neither of which are known, and the generation rate. This approach suggests that the rate equation for the defect density, N_D, is of the form,

$$dN_D/dt = \beta_{cr} N_H R - \beta_r N_H^* N_D \qquad (13)$$

where R is the electronic recombination rate (presumably proportional to electron and hole concentration), N_H^* is the concentration of excited mobile hydrogen, and β_{cr} and β_r are excitation and recombination rates, which probably contain time dependent dispersive factors.

The model also indicates that there is an upper limit on the metastable defect density which can be derived without knowledge of the rate constants. Only those weak bond states deeper than E_D are stable, because hydrogen in shallower states can migrate and presumably can recombine relatively quickly. Thus the upper limit on the metastable defect density is $\sim E_o N_H(E_D)$, which is about 10^{17} cm^{-3} at room temperature.

C. Hydrogen bonding configurations

The HDOS description of a-Si:H requires a detailed knowledge of the different possible hydrogen configurations. We have made total energy supercell calculations for various H configurations in crystalline Si evaluated within the local density

approximation (LDA). Because the local structure of c-Si is similar to a-Si, the average energies for >10 at. % H in a-Si:hydrogen will tend to be similar in the two systems. Refinements of the results to account for disorder are expected to be particularly important for low concentration configurations.

The calculations find that H pairs consisting either of an interstitial H_2 molecule (Fig. 7a) or H bound in an H_2* complex (Fig. 7b) are significantly lower in energy (1.6

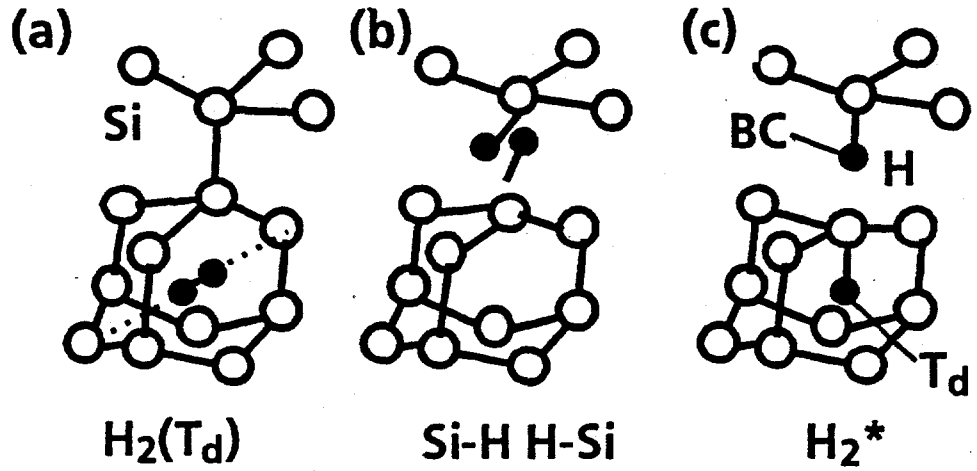

Fig. 7 Three possible diatomic H complexes in Si. (a) is the interstitial H_2 molecule located at the Td site. (b) Two H atoms bonded between the two Si atoms of an Si-Si bond. (c) The H_2* complex consisting of an H in the bond centered site (BC) and another in the T_d site.

and 1.2 eV per H pair, respectively) than isolated interstitial H. The H_2* complex consists of a Si-Si bond broken by H in a bond centered (BC) site while the remaining dangling bond moves to the back side of the Si atom where it is passivated by an H atom near the tetrahedral interstitial T_d site (Fig. 7c).

In Fig. 8, the energies from LDA calculations are depicted in terms of average energies per H atom in various configurations. While the absolute energies relative to H in vacuum may be in error by 0.3-0.4 eV, the relative errors are accurate to within 0.1-0.2 eV. The lowest energy site for an isolated H in a fully coordinated network is in the BC site and slightly higher in the T_d site (Fig. 8). The activation energy for diffusion of an isolated interstitial H in c-Si is estimated to be about 0.4-0.5 eV above the BC site indicated by the "percolation threshold" in Fig. 8. The energy of a Si dangling bond is about 2.3-2.4 eV below the percolation threshold. The H_2* complexes are particularly of interest because this configuration is the lowest energy configuration where H breaks a single Si-Si bond to form 2Si-H bonds.

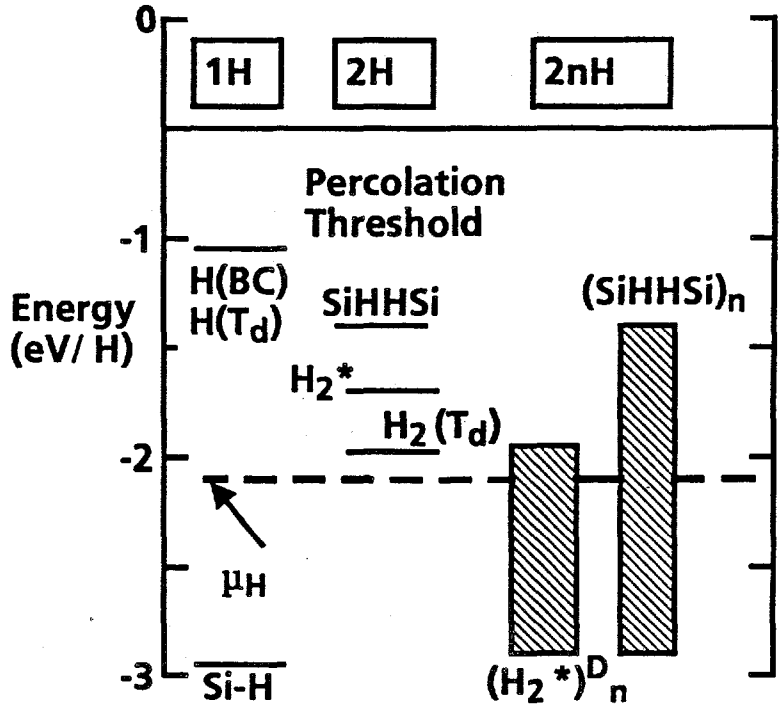

Fig. 8. Average energy of various 1H (neutral), 2H and 2nH configurations in c-Si per H atom relative to atomic H in vacuum from LDA calculations. The energy of extended configurations depend on platelet sizes and expansion of the platelets results in different energies. μ_H is an estimate of the H chemical potential.

This configuration by itself does not account for the clustered H phase or the H structure in a-Si:H but may explain metastable defect formation.

Additional calculations indicate that the H_2* complexes form larger clusters (Fig. 9). H_2 * complexes bind together with an energy of roughly 0.2 eV per H pair, because of the strained back bonds. If a large concentration of H is present, a 2-d extended platelet structure denoted by $(H_2^*)^D{}_n$ propagates along a local {111} plane where 2n is the number of H atoms in the platelet structure and D denotes the formation of a double layer of H (two H_2* per Si pair). Each additional H_2* relieves the strained backbonds near the perimeter of the platelet as it is incorporated into the structure (Fig. 9). The strained configurations near the edge are nearly H_2* configurations with a similar H binding energy representing higher energy H sites.

If the two surfaces of the platelet separate by about 0.3 nm or more, the energy of Si-HH-Si structure becomes comparable in energy to the H_2* platelet, and the platelets can evolve into a hydrogenated void, as shown in Fig. 9. This void consists of hydrogenated surfaces and possibly H_2 molecules internal to the void.

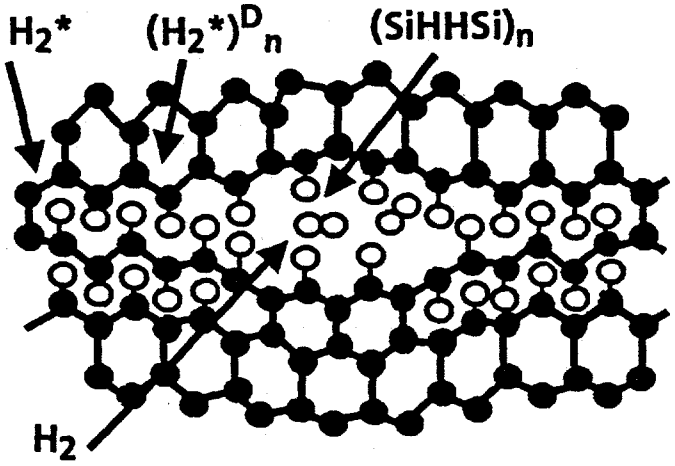

Fig.9 Possible structure of a planar platelet formed by H in Si. The edges contain Si-H bonds with strained backbonds. The interior sites are lower energy $(H_2^*)^D{}_n$ sites with binding energies up to 1.0 eV below interstitial H_2 molecules. For very large extended complexes or situations where there are voids or the Si lattice is under significant tension, a (SiHHSi)n configuration plus H_2 molecules in a void becomes comparable in energy to the $(H_2^*)^D{}_n$.

These different possible configurations of hydrogen suggest some new interpretations of experimental results in a-Si:H. We assume that the bulk of the H is bonded in extended $(H_2^*)^D{}_n$ complexes and a lesser amount is in more expanded SiHHSi complexes and isolated Si-H bonds. H diffusion occurs when single H atoms are excited to the percolation threshold from the edges of the platelet. These atoms then diffuse through the network until they reform in complexes or become trapped in the various available low energy sites.

NMR measurements provide information about the nearest neighbor H distances. The width of the line is inversely proportional to the cube of the distance to the nearest neighbor. The NMR spectra nearly always exhibit a two component central line. The narrow line indicates isolated H and the broad line results from clustered H. Irrespective of the deposition method or H content, the broad linewidth is near always about 25 ± 5 kHz. The two phases vary in relative concentrations but the relative H-H distance does not. From the structure of the platelet, the NMR linewidth is calculated to be 25 ± 4 kHz for 0.18 to 0.38 nm dilations of the platelet. Agreement between experiment and the expected linewidth demonstrates that the platelet structures are consistent with NMR experiments.

The platelet model described above is also consistent with H evolution experiments in a-Si:H deposited at low temperature. Such material exhibits two H

evolution peaks. The high temperature peak is consistent with monoatomic diffusion and scales with sample thickness. The low temperature peak arises from desorption of molecular H_2 into interconnected voids which communicate with the external environment. These voids collapse after H emission so that the monoatomic H evolved at high temperatures must diffuse through the bulk of the material to the top surface. This model requires that the voids collapse following H removal, experimentally demonstrating that the H provides an outward pressure on the void surface.

H diffusion experiments are also consistent with the platelet model. From the fact that roughly 1% of the H is in H_2 molecules, μ_H should be located somewhat below the interstitial H_2 molecule. Furthermore, while the precise path for creation of interstitial mobile H from platelets is unclear, the energy to remove much of the H from a platelet structure is near the H_2 interstitial as well. From both these considerations, the H diffusion activation energy should be on the order of 1.4-1.6 eV, ie. the energy difference between the percolation threshold and μ_H (Fig. 8).

The hydrogen diffusion coefficient and activation energy vary with Fermi energy (E_F) position, as shown in Fig. 10. H can diffuse either as H^+ or H^- depending on the Fermi level position, because the interstitial H possesses (0/+) and (0/-) transition levels at E(+/0) and E(-/0) within the silicon band gap. The energy, $E^{\pm}_p$ necessary to generate a mobile $H^{\pm}$ at the percolation threshold and the activation energy of the H diffusion coefficient, E_a, both depend on E_F according to the relation

$$E_a = E_P^{\pm} - \mu_H = E_P^0 - |E(\pm/0) - E_F| - \mu_H \qquad (13)$$

where E_p^0 is the percolation threshold of the neutral H. μ_H can be determined from Eq. (14) relative to the percolation energy (the dashed line in Fig. 10), from the experimental diffusion coefficient versus E_F, and from the calculated energies of interstitial H atoms at the BC and T_d sites. The dependence of the percolation energies on Fermi level overlap the data in Fig. 10 remarkably well and provide evidence that μ_H is located a few tenths of an eV below the interstitial H_2 near the unrelaxed platelet energies. The concentrations of H_2 and H_2^* are approximately consistent with the theoretical energies of the model and μ_H at this location. The increase of both the diffusion coefficient and metastability from doping is due to the lowering of the mobile H formation energy, and the diffusion is consistent with the platelet model and the energy calculations.

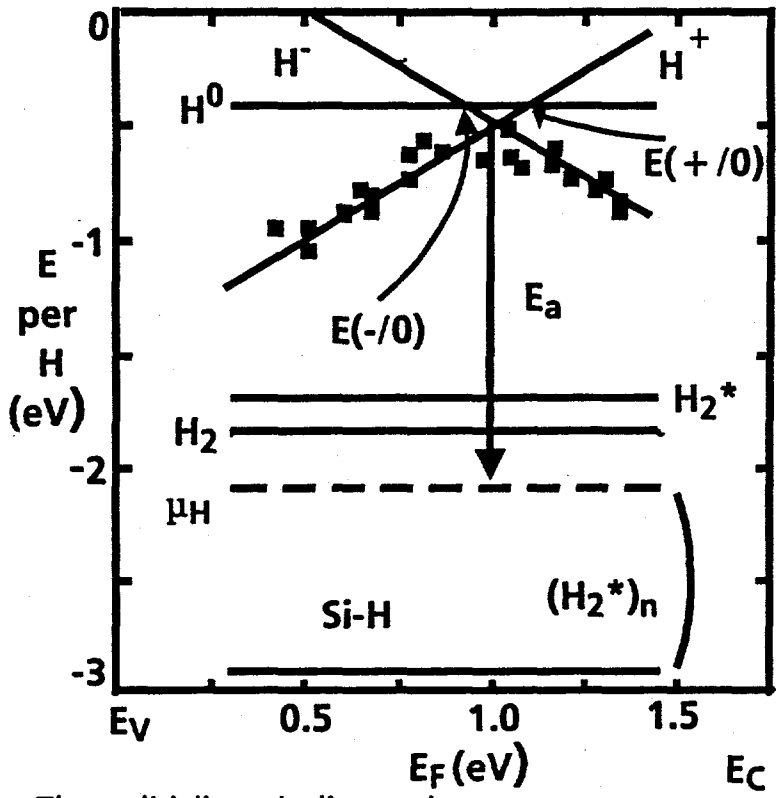

Fig. 10 The solid lines indicate the average energy per H for various configurations versus E_F. The 1H curves represent estimates of the percolation threshold for the various charged states of H obtained by adding 0.5 eV to the lowest stable energy sites for the isolated H. Data are taken from Beyer et al (J. Non-Cryst Solids 114, 217, 1989).

In conclusion, the platelet model can account for a number of experimental results concerning H structure, clustering and transport in a-Si:H. The H_2* not only serves as a building block for clustered H but also may be involved in metastability as well.

D. Model for the role of hydrogen complexes in the metastability

From the identification of various H bonding site energies described in the preceding section, one can identify probable configurations which may play a role in various H related effects such as H diffusion and metastability. A summary of the calculated energies relative to isolated H in vacuum for various configurations is presented in Fig. 8. From the activation energy of H diffusion, the chemical potential of H, μ_H can be estimated to be located 1.5 eV from the percolation threshold. The dominant H bonding configurations lie below μ_H while configurations above this level have reduced concentrations. From the energy diagram, the dominant H

bonding sites are isolated Si dangling bonds sites, the surfaces of open, self-sustaining voids, and the surfaces of platelets and other clustered forms of H which close following H removal. The latter two classes of sites may account for the broad line observed in H NMR of a-Si:H, while the narrow component arises from the isolated configuration. The interstitial H_2 molecule is somewhat above μ_H so it is present in reduced numbers.

Our calculations show that the H_2* complex dissociates in the presence of carriers (by the mechanism illustrated in Fig. 11 The two H atoms from the dissociation form

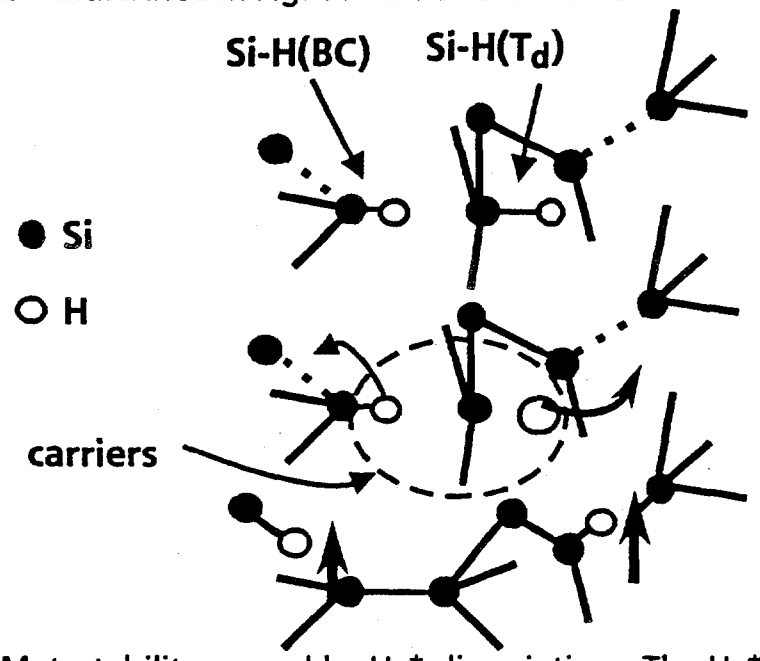

Fig.11 Metastability caused by H_2* dissociation. The H_2* captures carriers forming unpaired H atoms which diffuse to weak Si-Si bonds (dotted line) forming midgap defects.

1H configurations at weak bonds or surfaces creating dangling bonds. Recovery occurs when the single H configurations reform 2H complexes. The barrier to dissociation is on the order of 1.0-1.1 eV for capture of electrons or holes and 0.1-0.4 eV if both are simultaneously present.

Except for light-induced defect generation, metastability typically has generation and annealing energies of around 0.9-1.2 eV. Assuming that the rate limiting step for metastability is the formation of mobile interstitials, the states responsible are roughly of the H_2* type of configuration as shown in Fig. 7. These configurations are characterized by small clusters of paired H in positions which reform strong Si-Si bonds upon H removal. Light-induced defect formation is somewhat different in that the presence of both electrons and holes affords the possibility that both the

electron and hole contribute more energy to lowering the formation energy barrier than can be accomplished by single carriers alone. The effect reduces the interstitial formation barrier to a small value. Thus, the energy scheme suggests that the H_2* class of configurations are likely candidates for metastable defect formation in a-Si:H. Because these configurations are above μ_H, the number available for defect formation is small compared to the total H concentration thereby accounting for the relatively small number of induced defects ($<10^{18}$ cm^{-3}). The isolated Si-H bonds are apparently too strong to be involved in defect generation.

The H_2* platelet model therefore seems to be a viable candidate for metastability. The model as stated, differs slightly from the negative U model proposed by Zafar and Schiff because the defects in the negative U model arise from H leaving isolated dangling bond sites to form negative U pairs. The H_2* model could be altered to be consistent with this phenomenological model if one postulates that defect formation occurs when the carrier-induced H released from two isolated sites combines to form H_2* complexes without gap states. The problem with this model is that the energy of the Si-H bond is so large it is difficult to understand how carrier-dissociation can occur with such small activation energies. Furthermore, because the Si-H antibonding orbital is so much closer to the conduction band than the bonding level (-5 eV below the valence band edge), electrons would be expected to be much more effective for creating metastability than holes, contrary to observations. Nevertheless this may be possible on surfaces. Another closely related H model is the hydrogenated open void surface model. With the given numbers, the H bonding levels are too deep to account for metastability unless there are H transport pathways following the void surface which are significantly lower in energy than the percolation paths through the bulk. This scenario would require that the voids surfaces form an interconnected structure for macroscopic diffusion. However, diffusion is regarded as more or less uniform throughout the material. Furthermore, the hydrogenated Si(100)-like void surfaces should have H which is too close as indicated by H NMR indicating suppression of Si(100)-like surfaces. Without Si(100)-like surfaces, all H bonding would be nearly identical contrary to H evolution experiments indicating the presence of different phases. The void model however remains a possible contender for the structure of H in Si.

The proposed models have a number of implications for a-Si:H. If the H defect models are correct, metastability is intrinsic to the material and cannot be eliminated

by control of impurities unless such impurities significantly alter H bonding energies and structure. The models clearly indicate that to minimize metastability, one should strive to introduce enough H to passivate the isolated dangling bonds (improving carrier lifetime) and remove weak Si-Si bonds (increasing carrier mobility) but otherwise keep the H content low in order that the weaker H bonding configurations do not form. Hence, this model supports the recent ideas that the SiH2 concentration should be minimized and H content should be decreased to about 4 at. % or even somewhat lower. A number of studies have confirmed that lower H and SiH2 content films tend to exhibit smaller rates of metastable defect generation. Because H dilution and higher temperatures seem to lower the H chemical potential, deposition techniques incorporating these features should produce more stable films.

E. Hydrogen chemical potential and growth structure

We propose that equilibrium chemical reactions involving hydrogen are a major influence in determining the structure of a-Si:H during growth. The variations in structure are usually attributed to different gas radicals; SiH_3 is generally considered to be an important precursor to growth of good quality material, while SiH_2 or SiH are thought to result in poor material. Considerations of thermodynamic equilibrium and chemical bonding provide a different viewpoint. The equilibrium structure of a material is determined by a minimum of the free energy, independent of the growth process. Although an amorphous structure is not the equilibrium solid, it is reasonable to suppose that the structure in any small volume may represent a minimum free energy, subject to the constraints imposed by the long range disorder of the network.

The deposition model relates the chemical potential of atomic hydrogen in the plasma, μ_H, to the disorder of the film and explains the conditions for optimum film growth, the transition to crystallinity and the structure dependence of the equilibration rates. The deposition model is broadly based on the sequence of growth proposed by Gallagher and Scott (Solar Cells 21, 147 1987) in which SiH_x radicals attach to the growing surface, illustrated in Fig.12. Since the hydrogen concentration of the radicals is much larger than of the resulting film, Gallagher envisions a sub-surface region (with thickness, d_S, of order 10Å at usual growth temperatures) from which the excess hydrogen is eliminated.

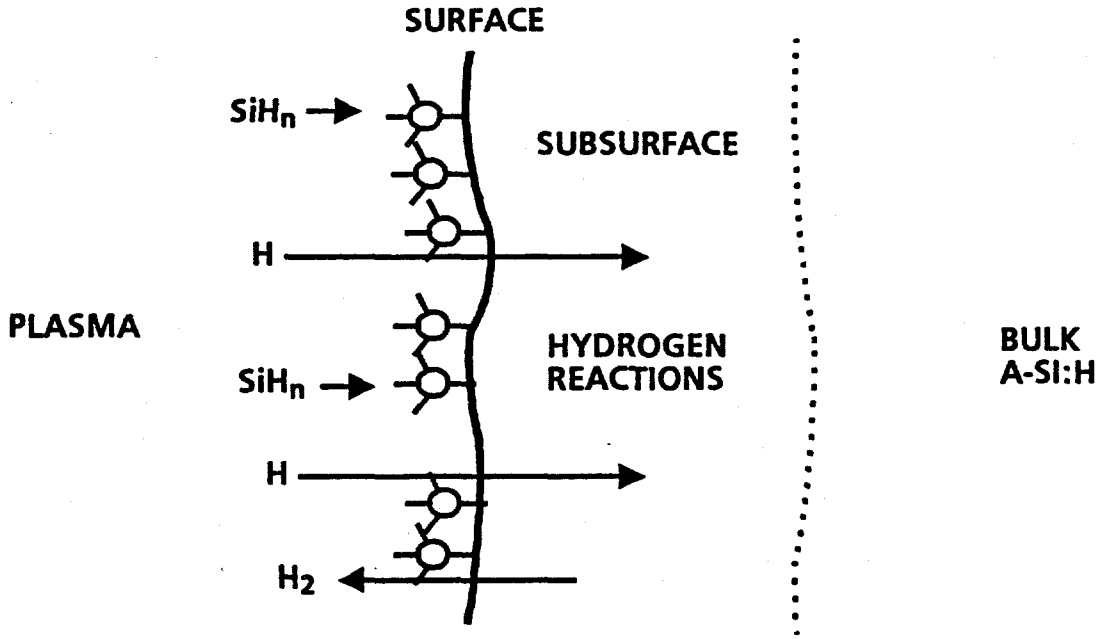

FIGURE 12. Schematic model for the attachment of silane radicals and hydrogen reactions at the growing surface of a-Si:H.

In plasma-assisted CVD, the plasma creates radicals which are not present in large quantity in the unexcited gas. Aside from silicon-containing radicals, the plasma creates atomic hydrogen whose concentration we describe by a chemical potential,

$$\mu_H = E_H + kT \ln (N_H/N_{Ho}) \qquad (14)$$

where E_H is the energy of atomic H in vacuum (see Fig. 6), N_H is the concentration in the plasma and N_{Ho} is the effective density of states (2.5×10^{24} cm^{-3} at 550K, the inverse of the quantum volume). The steady state hydrogen concentration is a balance between its creation by the plasma and its loss to various chemical reactions. The chemical potential in this situation is analogous to the quasi-Fermi energy defined for electrons in a photoconductor under illumination.

At the normal growth temperature, hydrogen diffuses within a-Si:H and redistributes between alternative bonding sites. Consequently, the hydrogen distribution is close to equilibrium and can also be described by a chemical potential. The interchange of hydrogen across the growing surface implies that the hydrogen chemical potentials in the plasma and the film tend to equalize; the main assumption of the model is that this process causes the hydrogen in the plasma to determine the atomic structure of the growing film.

The hydrogen chemical potential influences the network structure of a-Si:H. Atomic H forms a strong bond to silicon and the optimum structure is one which minimizes the hydrogen which is not strongly bonded to silicon. Thus, ideal bonding in a-Si:H consists of Si-Si and Si-H bonds, but not dangling silicon bonds or interstitial hydrogen. The bond angle and bond length disorder cause a distribution of Si-Si (and possibly Si-H) bond strengths. Figure 5a illustrates the hydrogen density of states distribution in a-Si:H. The weakest Si-Si bonds are closest to μ_H, since these are most easily broken by hydrogen through a reactions described in section 2A.

An Si-H bond which loses its hydrogen becomes a dangling bond, and a weak bond which gains a hydrogen atom results in a similar defect. A high density of both types of states at μ_H is therefore incompatible with the 8-N rule for chemical bonding. The immediate conclusion is that the optimum amorphous structure is formed when there is a minimum at μ_H in the hydrogen density of states distribution (see Fig. 13).

The minimization of the density of states at μ_H induces an interaction between the hydrogen and the silicon network structure. Accordingly, the growth reactions determine the structure by inducing a low weak bond density at μ_H. If the growth conditions are such that μ_H is raised, the bonding structure is no longer in a stable state and there is a tendency to change the distribution of Si-Si bonds by breaking weak bonds and reconstructing the network to give either Si-H bonds or stronger Si-Si bonds. The different network structures which follow from a change in μ_H are illustrated in Fig. 13.

The weak bond model assumes an exponential distribution of weak Si-Si bonds,

$$N_{wb}(E) = N_o \exp[-(E_S-E)/E_o]\,; \qquad E<E_S \tag{15}$$

where E_S is indicated in Fig. 13 and is approximately the energy of hydrogen in a normal Si-Si bond, and E_o is the slope of the distribution. A density of weak bond states, N_{min}, at μ_H then gives,

$$E_o=(E_S-\mu_H)/\beta, \text{ where } \beta=\ln(N_o/N_{min}) \tag{16}$$

E_o is a measure of the structural disorder of the material and in the weak bond model is related to the slope, E_V, of the exponential valence band tail, which has a density of states proportional to $\exp[-E/E_V]$. Equation 16 is doubtless approximate, but illustrates the nature of the relation between structural order and μ_H.

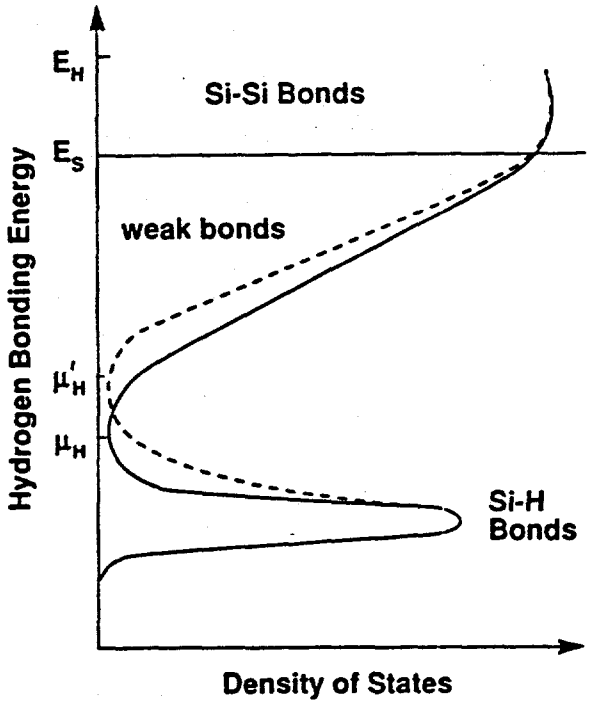

Fig. 13. The hydrogen density of states distribution showing the modified density of states when the chemical potential is changed.

The position of the H chemical potential is not the only constraint on the structural disorder. An unhydrogenated amorphous silicon network has a high bonding disorder, because a 4-fold coordinated network is overconstrained. The inclusion of hydrogen relaxes the network and reduces the disorder. Many measurements show that the band tail slope, E_V, can be reduced to 45-50 meV, but no a-Si:H films exist with substantially smaller values. We infer that there is a minimum disorder in a-Si:H. Figure 14 illustrates the region of allowed a-Si:H structures, based on this reasoning. The boundary line limits the possible structures, which are constrained to have a higher disorder at very low hydrogen concentrations (and possibly also at high hydrogen levels). Hydrogenated crystalline silicon lies in a separate region of the space. Following the arguments used to obtain eqs. 15 and 16, we associate the structural order with the energy of μ_H, such that a high order corresponds to a high chemical potential of H, as shown in Fig 14.

The growing film surface is assumed have a high hydrogen concentration and a high disorder, both originating from the attachment of SiH_x radicals; this starting point is illustrated by the circle in Figs. 14 and 15. During the subsurface reactions, the structure follows a trajectory of H concentration and structural order, towards a stable structure determined by the position of μ_H. The model does not consider the

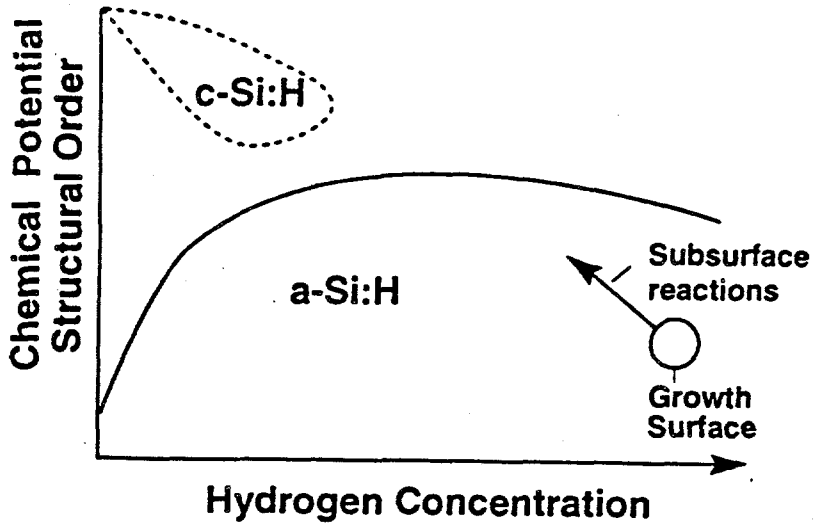

Fig. 14. Illustration of the range of allowed structural order and hydrogen concentration of a-Si:H and crystalline silicon (c-Si:H). The position marked by the circle corresponds to the surface structure during growth, and the dashed line illustrates the change in structure induced during the subsurface reactions. The H chemical potential is an equivalent measure of order, as described in the text.

specific reactions, but there is evidence that bonded hydrogen in the film is removed by reaction with hydrogen from the plasma.

The present model identifies three broad regions of growth, illustrated in Fig. 15, as follows;

A. Kinetically limited growth (Fig. 15a). Low temperature growth results in defective material because hydrogen is not properly equilibrated due to its low diffusion coefficient. The H content and the disorder are higher than for an ideal a-Si:H film because the equilibration reactions cannot occur. Subsequent annealing of the film improves the structural order and reduces the defect density, without changing the hydrogen concentration (see Fig. 15a). The annealing effect is a well known phenomenon in films deposited below about 200 °C.

B. Amorphous structures determined by μ_H (Fig. 15b). At higher temperatures, the H diffusion is fast enough to allow the film structure and H content to be determined by the chemical potential. We expect that the surface reactions first establish a structural order determined by μ_H, and then continue to remove hydrogen until constrained by the inability of very low hydrogen concentration films to maintain the same structural order; these two processes are illustrated in Fig. 15b. Optimum films require a sufficiently high μ_H so that the structure reaches the limits

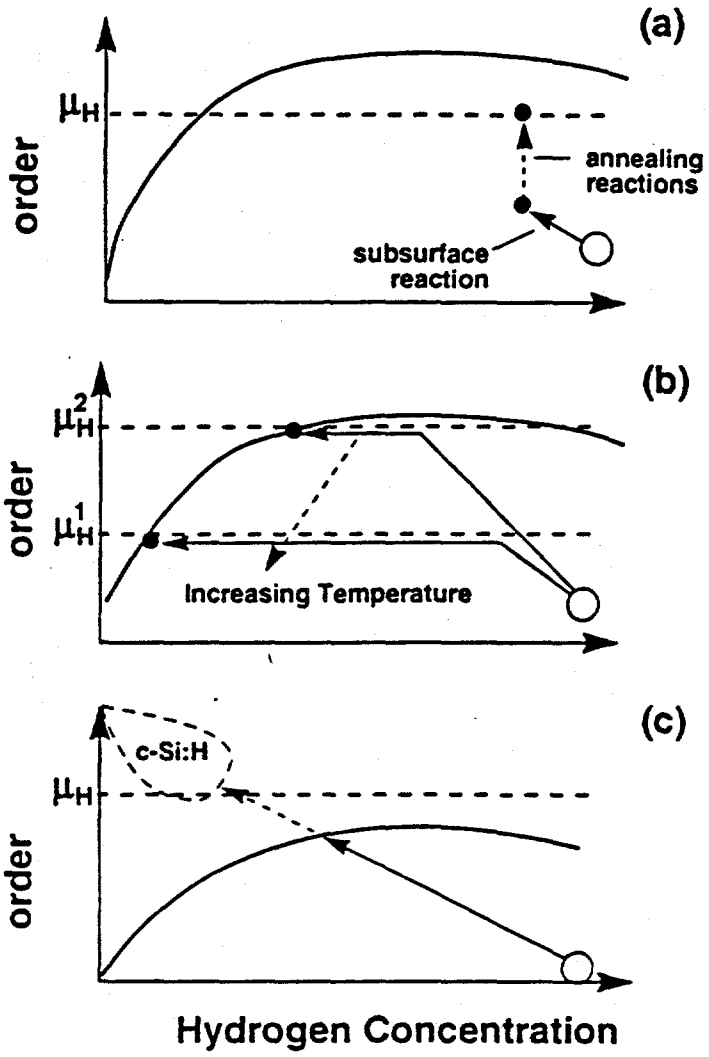

Fig. 15. Illustrations of the various hydrogen-induced structural reactions, showing three types of growth, as described in the text.

imposed by the network disorder. A higher temperature reduces μ_H, and therefore induces a more disordered film and a lower hydrogen concentration. Optimum films are therefore grown at the lowest temperature at which the kinetic limitation can be avoided. Our model further predicts that high temperature growth (>300°C) benefits from a high hydrogen concentration in the plasma gas and increased rf power. In contrast, at deposition temperatures of 250°C or below, the increased growth rate of a high rf power causes kinetically limited growth.

C. Instabilities at high μ_H (Fig. 15c). A sufficiently high hydrogen chemical potential leads to an unstable situation, because the degree of structural order determined by

μ_H greatly exceeds that available in the amorphous network. As shown in Fig. 15c, μ_H does not intersect the range of structures available to a-Si:H material. We propose that this is the condition necessary for a transition to growth of crystalline silicon. The model suggests that the transition to crystalline growth is enhanced by high H concentration in the plasma, high rf power and low temperature, since all three raise the chemical potential. These are indeed the observed conditions, although the films revert to being amorphous at low temperature because the H diffusion rate is too low to allow equilibration. The predicted suppression of microcrystallinity at high deposition temperature is observed.

3. DEFECTS AND ELECTRONIC PROPERTIES

We continue to study the electronic properties of a-Si:H, particularly to understand defects and their role in the metastability phenomena. A new technique has been developed which obtains the density of deep defects, by measuring the reverse current of p-i-n devices. Besides being a measure of defects, this technique explores the electrical properties of solar cell devices in greater depth than previously. We have also investigated the role of potential fluctuations in compensated a-Si:H.

A. Thermal generation currents in p-i-n diodes

Measurements have been made of the I-V characteristics of p-i-n devices of 1μm thickness. Fig. 16 shows the dependence of the room temperature dark current on the time after the voltage is applied, for different reverse bias voltages. The current decreases slowly by about an order of magnitude, over a period of 5-300 sec, and continues to decrease for about 15-20 minutes when further changes are imperceptible. There is an additional order of magnitude decreasein current in the time range between 0.01 and 5 sec. The steady state current is approximately 10^{-11} A/cm^2 at 1V. The current measured at 300 sec is larger by only 50% at 4V and by a further factor of 5 by 12V. A similar slow decay of the reverse bias current is observed after illumination.

The dark current is identified as the bulk thermal generation current from defect states in the gap. The thermal generation current, I_{th}, arises from the excitation of electrons from the valence band to the empty gap states, and from the filled states to the conduction band. The contribution to the generation current from a single trap level is given by the Shockley-Read-Hall formalism. Fig. 17 shows a schematic

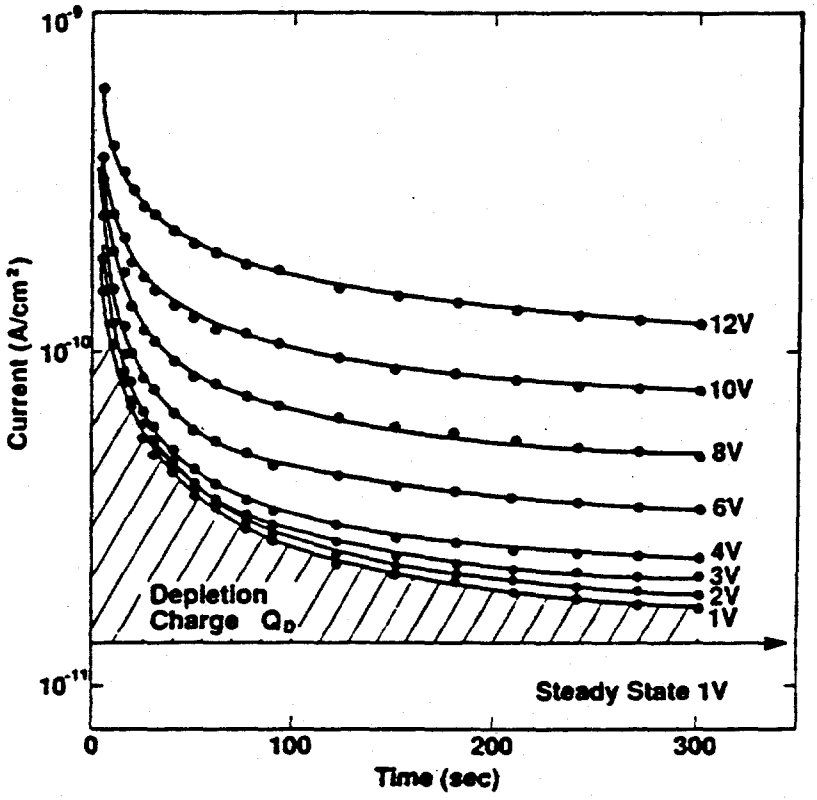

Fig. 16. Decay of the current after a bias volage is applied, for volatges from 1 to 12 V. The steady states current at 1V is shown, and the shaded area represents the bulk depletion charge.

diagram of the density of states distribution, N(E), of a-Si:H showing the broad band of defect states near the middle of the gap. For a continuous distribution of traps, the generation current is dominated by the emission from those traps within kT of an energy E_{FD}, for which the excitation rates for electrons and holes are equal. The thermal generation current, assuming full depletion and complete collection of excited electrons and holes is,

$$I_{th} = e\, N(E_{FD})\, kT\, \omega_o \exp[-(E_C - E_{FD})/kT]\, A\, d \qquad (17)$$

where $\omega_o \sim 10^{13}$ sec^{-1} is the excitation rate prefactor, A is the area and d the thickness. E_{FD} is a quasi-Fermi energy defining the occupancy of the localized states near mid-gap, and is determined by the thermal generation process. The condition of equal electron and hole generation places E_{FD} very close to half way between the valence band and conduction band mobility edges. The rate prefactor is different for electrons and holes because of their different capture cross-sections, σ_e and σ_h, which shifts the quasi-Fermi energy to,

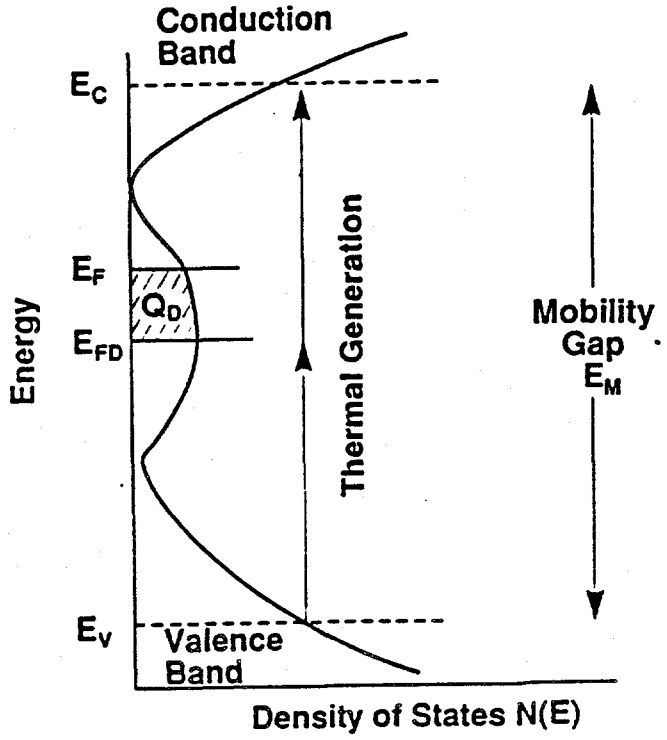

Fig. 17. Density of states diagram showing the origin of the thermal generation current through gap states. The shaded region represents the depletion charge.

$$E_C - E_{FD} = \tfrac{1}{2}E_M + \tfrac{1}{2}kT \ln(\sigma_e/\sigma_h) \qquad (18)$$

where E_M is the mobility gap energy. Since σ_e/σ_h is of order 0.1, the shift is negative and roughly 20-40 meV. For a mobility gap of 1.9 eV, E_C-E_{FD} is therefore expected to be 0.9-0.95 eV.

The equilibrium Fermi energy, E_F, of undoped a-Si:H at zero bias is above mid-gap by $\Delta E = 0.1$-0.2 eV. The thermal generation electron current therefore initially exceeds I_{th}, and is given by,

$$I_{th}(0) = I_{th} \exp(\Delta E/kT) \qquad (19)$$

The decreasing electron current seen in Fig. 16 is explained by depletion of electrons from the undoped layer. The depletion charge is,

$$Q_D = e \int_{E_{FD}}^{E_F} N(E) \simeq N(E_{FD})\,\Delta E \qquad (20)$$

where the second expression makes the approximation that N(E) is constant in the energy range between E_F and E_{FD}, which is expected to be a reasonable assumption since neither E_F or E_{FD} are within the band tails. The depletion charge is represented by the shaded area in Fig. 17.

The thermal generation current decreases after the voltage is applied, from the initial value $I_{th}(0)$ to the steady state current, I_{th}. The decay time constant is,

$$\tau = \omega_o^{-1} \exp[(E_C - E_F(t))/kT] \qquad (21)$$

The decay is non-exponential because the Fermi energy is time dependent and moves from E_F to E_{FD} during charge depletion. When the steady state current is subtracted, the longest room temperature time constant, τ_{max}, is 200-300 sec, and corresponds to an energy $E_C - E_{FD} \approx 0.9$ eV. The temperature dependence of the depletion current confirms that both I_{th} and τ are thermally activated with energy 0.9 ± 0.03 eV, as shown in Fig. 18 in agreement with the expected value. The shorter

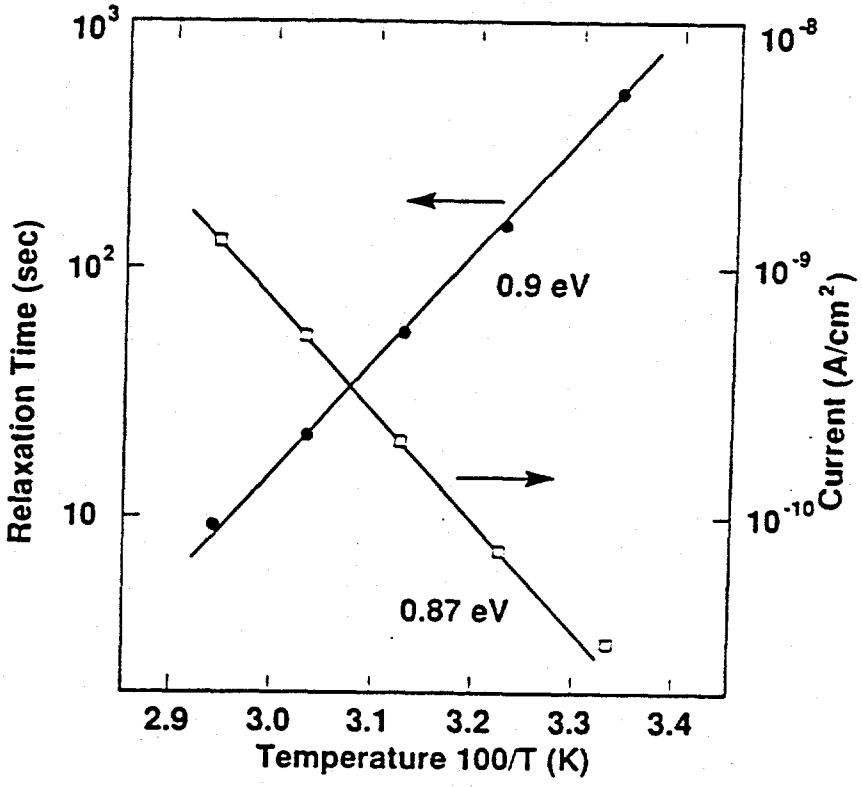

Fig. 18. Temperature dependence of the reverse current decay time and of the steady state current, showing thermally activated behavior with similar activation energies as indicated.

initial decay time of 1-10 sec is consistent with E_C-$E_F(0) \simeq 0.75$-0.8 eV.

Fig. 19 shows the bias voltage dependence of the steady state current, measured at least 15 minutes after the voltage is applied. In the annealed state, the current

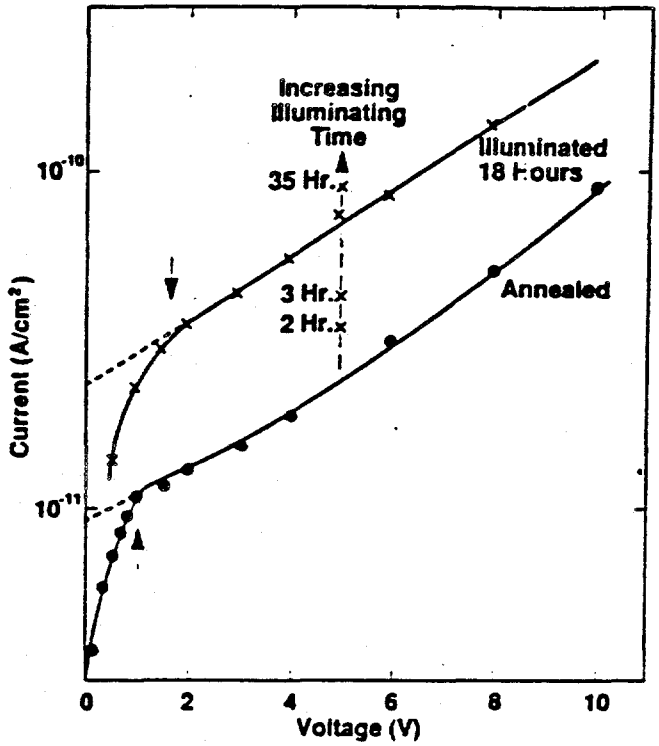

Fig. 19. Voltage dependence of the steady state thermal generation current, showing the effects of prolonged illumination, which generates excess states in the gap, and a correspondingly larger current. The arrows indicates the bias at which the sensor is fully depleted. The effects of light exposure are also indicated

increases rapidly from 0 to 0.7V. The voltage dependence arises because the generation current is approximately proportional to the fraction of the sample for which the electron occupancy is described by the quasi-Fermi energy, and this fraction increases rapidly at low bias. Depletion is indicated by the arrows in the Figure 19 at the change in slope of the I-V characterisics. In the voltage range 1-4V, the sublinear increase in current is expected for a bulk generation current. Although equation 18 indicates that the generation current has no voltage dependence, it is enhanced by field-assisted excitation, as described below.

The thermal generation current is proportional to the density of deep states $N(E_{FD})$. Light soaking is known to reversibly induce defects in a-Si:H with a time dependence obeying a $(\text{time})^{1/3}$ law. Fig. 19 shows that prolonged exposure to white light increases the dark current while maintaining the same voltage

dependence. The increase follows the $t^{1/3}$ law, confirming that bulk defect states are the origin of the current. Annealing at 150°C restores the current to its original value.

The thermal generation model quantitatively accounts for the dark current. Combining eqs 17, 20 and 21, gives.

$$I_{th} = Q_D kTAd/\Delta E\tau_{max}. \quad (22)$$

Thus the thermal generation current is given in terms of the depletion charge and the current decay time. The ionized defect density, $N(E_{FD})\Delta E$, of depleted p-i-n samples is reported to be $6\text{-}8\times10^{14}$ cm^{-3}, and the excess charge represented by the shaded area of Fig. 17 is consistent with this value. Combining this with an estimated $\Delta E = 0.1$ eV, $\tau_{max} = 200\text{-}300$ sec, and a film thickness of 1 μm, leads to a predicted thermal generation current of,

$$I_{th} = 0.8\text{-}1.6 \times 10^{-11}\ A/cm^2 \quad (23)$$

The agreement with the measured value of 1×10^{-11} A/cm^2 is excellent considering the uncertainties in the exact decay time and in ΔE.

B. Field dependence of the generation current

The thermal generation model outlined above has no voltage dependence to I_{th}, provided that the sample is fully depleted and the quasi-Fermi energy is at E_{FD} throughout the sample. In practice, there is a significant voltage dependence, shown in Fig. 20. The field enhanced emission which increases the current due to an lowering of the effective excitation energy. Such a field dependence is described by a tunnelling factor $\exp(-\beta_t F)$, for excitation of a particle from an initially charged defect, or by a Poole-Frenkel mechanism for a neutral defect which enhances the rate by $\exp(-\beta_p F^{1/2})$, where F is the field. Detailed analysis of the field dependence is complicated by the presence of the band tail localized states and by the fact that both carriers are excited from the same defect. The field dependence of the energy is defined as,

$$E_C - E_{FD} = (E_C - E_{FD})_o - E_L(F) \quad (24)$$

where F is the field, and is assumed to be uniform in the sample (i.e $F = V/d$). The reduction, E_L, of the emission energy may be estimated from the data using eqs. 17 and 24,

$$E_L(F) = kT \ln \frac{I_{th}(F)}{I_{th}(0)} \qquad (25)$$

Fig. 20 shows the voltage dependence of E_L deduced from the data in Fig. 19. E_L is referenced to the generation curent at 1V bias, since the value of $I_{th}(0)$ cannot be directly measured. E_L shows an approximately linear increase with applied voltage to a value of 50 meV at 10V.

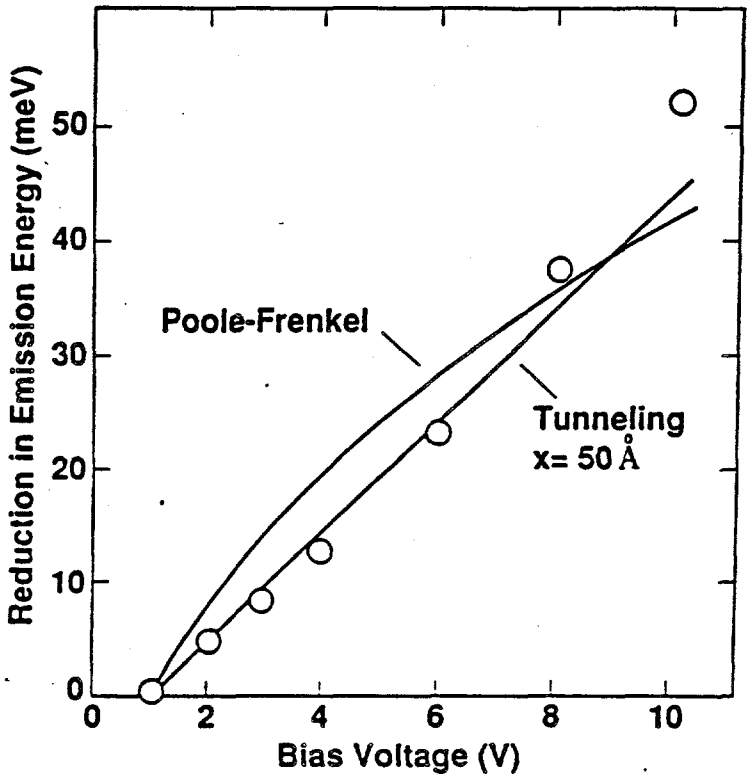

Fig. 20. The field reduction in the emmisison energy deduced from the voltage dependence of the generation curent. The lines show the predictions of simple models of the energy reduction due to tunelling and the Poole-Frenkel effect.

The field enhancement of the emission rate could be due to either tunnelling or a Poole-Frenkel effect. The tunnelling mechanism applies when the defect is intially charged so that the electron leaves a neutral defect, while the Poole-Frenkel model applies when there is a Coulomb interaction between the defect and the emitted particle. Tunnelling lowers the emission energy by,

$$E_L = F R_T, \qquad (26)$$

where F is the field and R_T is the tunnelling length. The data in Fig. 20 suggest a tunnelling length of about 50Å. The extent of the wave function of band tail

carriers is estimated to be about 10Å, so that this tunnelling distance seems reasonable. The barrier lowering in the Poole-Frenkel model is

$$E_L = 2\left[\frac{eE}{4\pi\varepsilon\varepsilon_o}\right]^{\frac{1}{2}} \tag{27}$$

Equation 27 gives a value for E_L which is comparable with the data in Fig. 20, although the square root dependence on field is not given correctly by the data. However, both the electron and hole emission are affected by the field and one of these transitions is subject to a Coulomb interaction while the other is not, depending on the intitial charge of the defect and the order in which the electrons and holes are emitted. Since the two emission rates must balance, the position of E_{FD} adjusts to correct for any difference in the rates induced by the high fields, and this effect complicates further analysis. We conclude that the observed voltage dependence is consistent with the expected field induced lowering of the emission energy.

C. Metastability effects at contacts

The dominance of thermal generation in the reverse current of p-i-n devices implies that any contribution to the reverse current from carriers injected across the contact is significantly lower. However, some devices of the same structure have a larger reverse current which is identified with contact injection. The distinguishing characteristic is a current which increases with time after the voltage is applied. The increase is associated with the depletion of charge from the i layer, which changes the field profile and results in a time dependent increase in the electric field at the p-i interface. The contact injection current increases with the field at the contact, accounting for the different time dependence. The contact current seems to originate from a defective p-i interface, but the nature of the defect is presently unknown.

The exact form of the time dependence varies markedly from sample to sample and also depends on the thermal history. Fig. 21 shows a sequence of measurements of the time-dependent current, illustrating metastable changes which depend on bias and annealing. The sample is initially in a rested state, having been held in the dark for many days. The reverse bias current transient has a brief initial decay due to charge depletion, but after a few seconds the current begins to increase slowly. The voltage was applied for 20 minutes, after which the current had increased by about

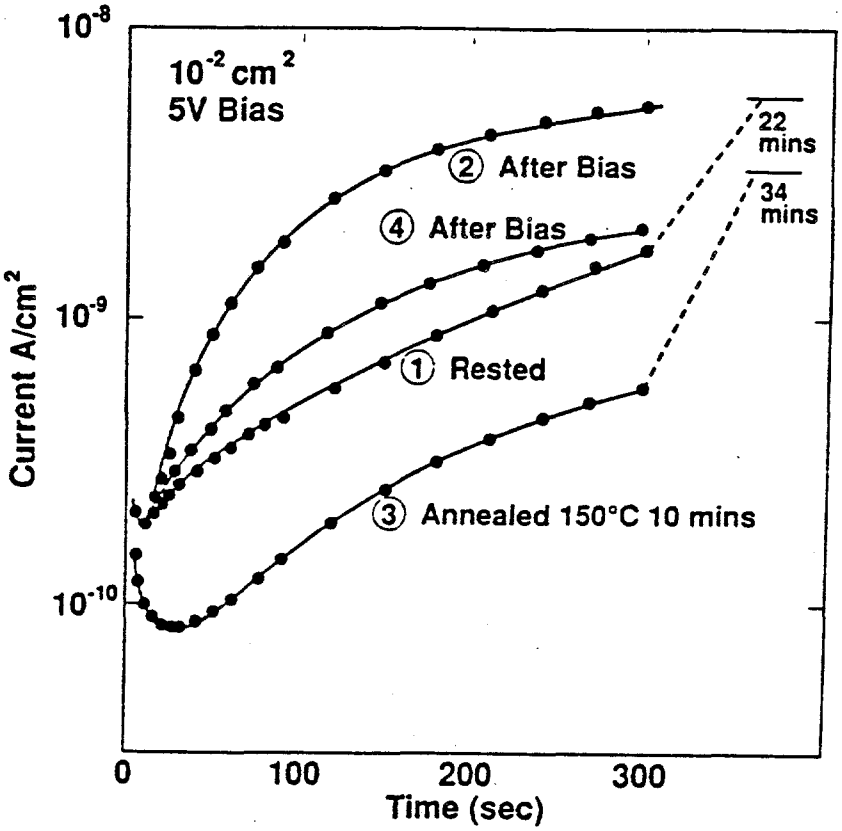

Fig. 21. Time dependence of the contact injection current showing metastable changes in the current induced by prolonged bias. The numbers indicate the sequence of measurements as discussed in the text.

an order of magnitude, but had still not completely stabilized. Next the reverse bias was removed and the sample kept at zero bias at room temperature for several minutes, to allow the depletion charge to return and the sample to reach electronic equilibrium. When the experiment was repeated, the current had a different time dependence; it increased more rapidly and levelled off at about the final current in the first measurement. The sample was then annealed at 150°C for 10 minutes. The subsequent reverse bias transient resembled the initial one, with a very slow current increase, although the data were not exactly the same. This cycle of annealing and biassing could be repeated, and shows that there is a metastable change in the sample properties induced by the long-time application of a reverse bias.

Other results show that annealing progressively removes the high reverse current induced by a long bias. It is also evident that the annealing behavior is different at short and long times, so that that the overall effect is rather complicated. The main observation, however, is that there is a metastable change in the reverse current, induced by bias, which has approximately the same annealing temperature as the

many other metastable defect creation processes observed in a-Si:H. These changes are only observed in samples exhibiting reverse currents dominated by contact injection

The metastable changes at the long time scale are too slow to be explained by the depletion charge, and also recover too slowly after the bias is removed. Instead, the changes are attributed to bias-induced defect creation, probably near the p-i-interface. Such a mechanism is known to occur in a-Si:H when the Fermi energy is moved from its equilibrium position by bias or current flow. The defect creation rate is known to be slow, with annealing at 100-200°C, thus exhibiting the same general characteristics as found in the present experiments. However, it is unclear exactly where the defects are created. Assuming that current injection is at the p-i interface, the change may occur in either of these two layers. Defect creation in the undoped layer may be anticipated because the Fermi energy is moved from mid-gap in the region very close to the p-layer. Any bias induced defects cause an increase in the field at the contact and so can explain the increase in the current. The bias-induced effect may originate in the p-layer, since the doping efficiency increases and the defect density may decrease when p-type material is biased into depletion. It is not immediately clear how this change would increase the injection current, but some effect seems plausible.

D. Potential fluctuations in compensated a-Si:H

Potential fluctuations in compensated hydrogenated amorphous silicon have been investigated by comparing data on the mobility of both electrons and holes with the optical absorption edge. Electron and hole drift mobilities were obtained using time-of-flight (TOF) transient photocurrent measurements over a range of applied fields. The variation of charge collection with electric field was recorded to ensure that the transit time data were taken in a region of full charge collection. The transit times were identified from the change in slope of the time dependence of the current, and were confirmed by the dependence of the transit time on applied field.

The variation in electron and hole mobility with doping is shown in Figure 22 The electron mobility drops from about 1 cm^2/Vsec in undoped a-Si:H to $3x10^{-6}$ cm^2/Vsec at high doping levels, with the largest change occuring at doping levels between 10^{-4} and 10^{-3}. Although the electron and hole mobilities differ by two orders of magnitude in undoped a-Si:H, they approach similar values in heavily

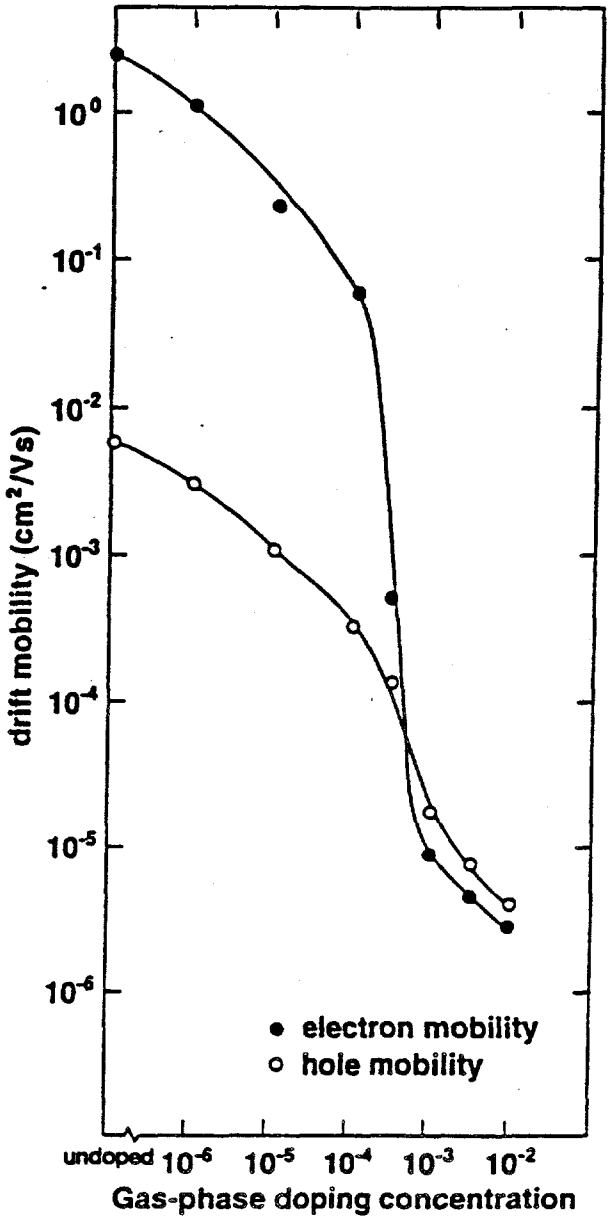

FIG. 22. Dependence of the room temperature electron and hole drift mobilities on compensation level in a-Si:H. An average mobility is shown for applied electric fields which range between $2x10^3$ and $5x10^4$ V/cm.

compensated material having a gas phase dopant concentration of 10^{-3} or greater. This behaviour suggests that the mechanism suppressing the mobility affects both signs of carrier in a similar manner. The temperature dependence of μ_{DE} and μ_{DH} was measured on some samples. Samples with the lower mobilities gave a higher activation energy as expected from multiple trapping, with values of about 0.6 eV at the highest doping levels.

The absorption edge was measured using optical transmission for energies above 1.6 eV and photothermal deflection spectroscopy (PDS) for energies between 0.7 eV

and 2.0 eV. The optical absorption edges for several different doping levels are shown in figure 23 which plots the absorption coefficient, α_A, against energy. The exponential region of the absorption edge at low compensation is almost identical to that for undoped material, showing very little change until the dopant concentration exceeds 10^{-4}. A large shift in the absorption edge is observed in samples having dopant concentrations greater than 10^{-4}. The broadening of the absorption edge is expressed in terms of the slope of the exponential edge, E_0.

$$\alpha_A = \alpha_o \exp(E/E_o) \tag{28}$$

where α_A is the absorption coefficient. The value of E_0 reaches 130 meV for compensation of 10^{-2} but remains around 55 meV for compensation up to and including 10^{-4}.

The decrease in drift mobility and the related increase in activation energy is due to trapping of carriers in states with increasing binding energy. Two alternative

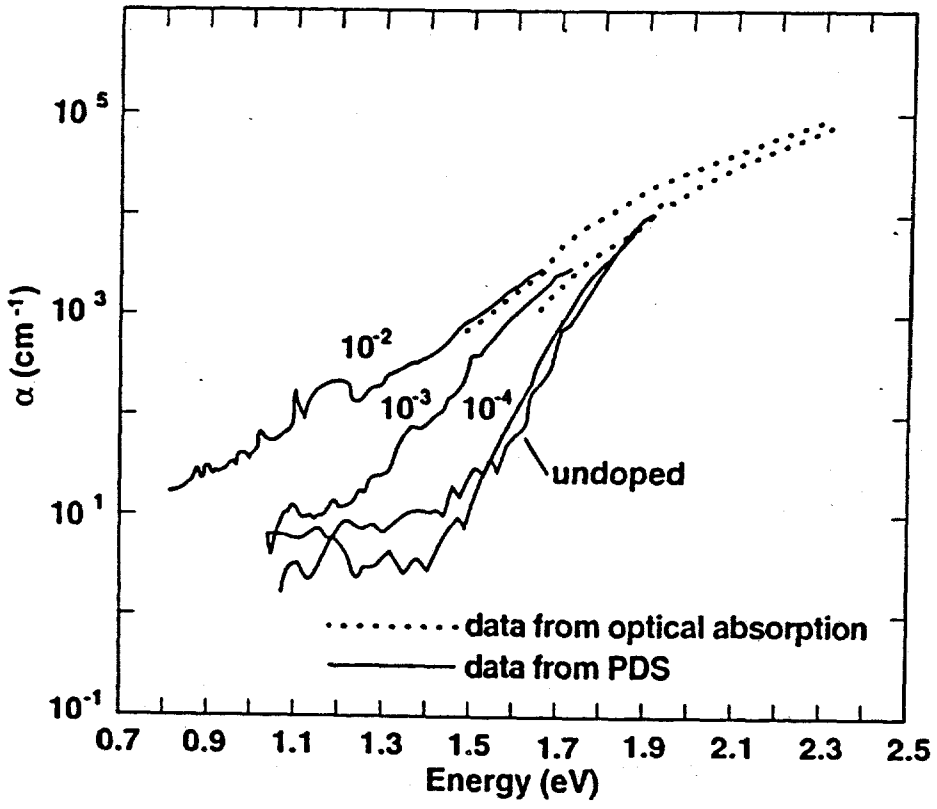

FIG. 23. The optical absorption coefficient as a function of photon energy for various compensated samples.

explanations for the traps are considered here; broadening of the band tail distribution and the presence of long range potential fluctuations. While it is difficult to distinguish between these models from the mobility data alone, they give different predictions for the shape of the optical absorption edge.

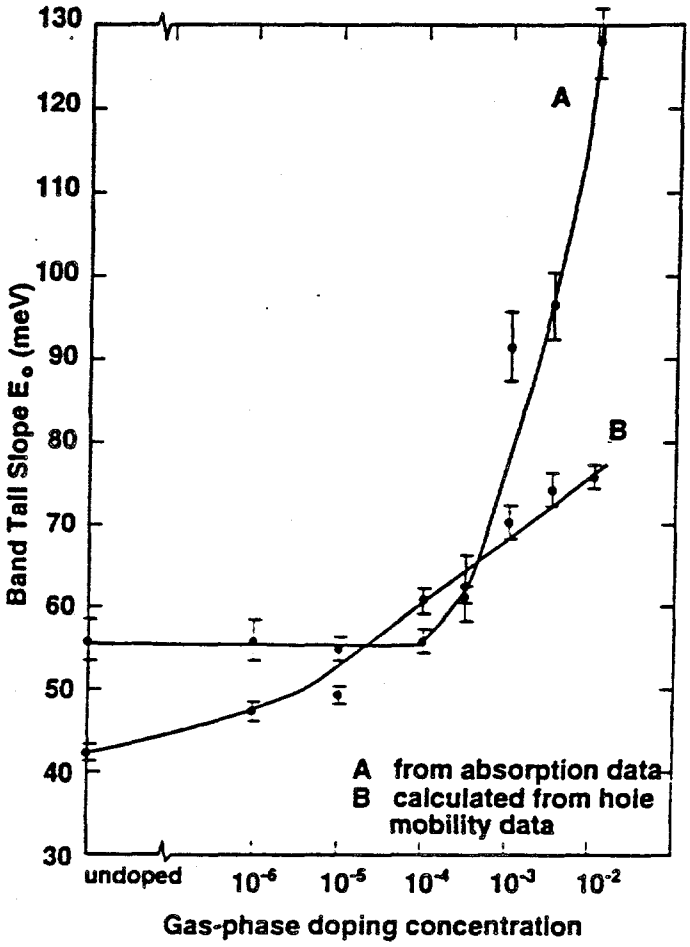

FIG. 24. Dependence of the absorption edge slope on compensation level; (A) from optical absorption data and (B) calculated from the hole mobility.

In the multiple trapping model, the decrease in carrier mobility is a result of trapping by a broadened distribution of band tail states. Increased compensation is assumed to introduce deeper traps, which progressively reduce the carrier mobility. The mobility is related to the slope of the exponential band tail, and the value of kT_V derived from hole mobility data should agree with the slope of the band edge, E_o, observed directly in optical absorption measurements. Figure 24 plots the slope of the band tail against increasing dopant concentration. Curve A shows the change in the band edge slope as measured directly from the slope of the optical absorption

tail. Curve B is calculated from the measured hole mobility using the relationship derived by Tiedje and Rose,

$$t_T = \frac{1}{\omega_o}\left[\frac{\omega_o}{2(1-a)}\right]^{\frac{1}{\alpha}}\left[\frac{L}{\mu_o}\right]^{\frac{1}{\alpha}} \qquad (29)$$

where t_T is the carrier transit time, ω_o, is the attempt-to-escape rate ($\simeq 10^{12}\ s^{-1}$), L is the sample thickness, E is the electric field applied during TOF measurement, μ_o is the free carrier mobility, and α is related to the slope of the band edge, kT_V, ($\alpha = T/T_V$). The value used for the free carrier mobility was 10 cm^2/Vs.

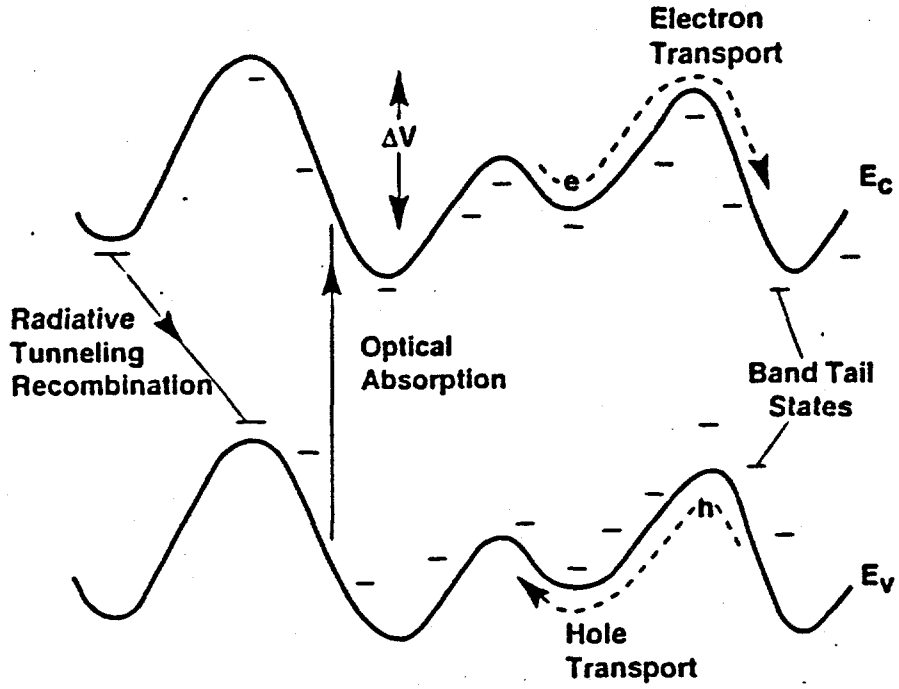

FIG. 25. Model of long range potential fluctuations, illustrating the magnitude of the fluctuations, ΔV, the electron and hole transport paths, the vertical optical transitions and the tunnelling ratiative recombination transition.

The two measurements of the band tail slope in Figure 24 are inconsistent for the compensated samples, and suggest that the band tail broadening model does not apply. Undoped a-Si:H has an absorption slope of 55 meV and a value of 45 meV from time-of-flight. This difference is consistent with the band tail model, and occurs because the absorption is a convolution of the valence and conduction bands, and consequently is slightly broader than the valence band tail. The optical absorption data shows that the band tail slope is unchanged in compensated a-Si:H for dopant concentrations up to 10^{-4}, but rapidly broadens at higher compensation.

In contrast, the mobility data when analyzed within the model of band edge broadening suggests that the valence band tail becomes broader with increasing compensation, even at low doping levels when there is no change in absorption.

The dopant atoms in compensated material give rise to local charge centers because both the donors and acceptors are ionized. When the compensation level is high enough, the number of free carriers available in the material is not sufficient for complete screening, and the random charge centers act as sources of long range potential fluctuations. The reduction in mobility with compensation is explained by the confinement of the carriers in the potential wells of the fluctuations, as indicated in Fig. 25.

Estimates of the electrostatic field which may be expected to arise as a result of potential fluctuations in compensated material, follow the approach used by Beyer and Overhof. Within a volume L^3, the statistical fluctuation in charge is given by $(NL^3)^{1/2}$ where N is the total number of ionized dopant atoms per unit volume. The potential fluctuation, $\pm \Delta V$, arising due to this fluctuation in charge is given by,

$$\Delta V \simeq \frac{(NL^3)^{1/2}}{4\pi\varepsilon\varepsilon_o L} \tag{30}$$

The magnitude of the fluctuations are limited by the screening length, L_s, so that,

$$\Delta V \simeq \frac{(N^{1/2} L_s^{1/2})}{4\pi\varepsilon\varepsilon_o} \tag{31}$$

Normal screening by free carriers is weak because of the low conductivity of compensated a-Si:H. Instead, screening occurs when the potential fluctuations are sufficiently large that the Fermi energy approaches one of the band tails and there is locally a high carrier concentration. In this situation the magnitude of the potential fluctuations changes little with doping level, having a value, ΔV_{max}, approaching half the band gap energy,

$$\Delta V_{max} = \pm \frac{1}{2}\left(E_G - \Delta E_G - \Delta E_V \right) \approx \pm \text{ (0.5-0.6) } eV \tag{32}$$

where ΔE_C and ΔE_V are the energies between the Fermi energy and the mobility edges at the peak of the fluctuations, determined by the need to provide sufficient carriers to screen the fluctuations. We estimate that $\Delta E_C \simeq 0.2$ eV and $\Delta E_V \simeq 0.4$ eV,

and note that these energies change little with doping because of the steep increase in the band tail density of states. These values agree with the activation energy of the drift mobility at high doping levels.

When the fluctuations have reached their maximum voltage range, constrained by the band edges, the main doping dependence is in the spatial period of the fluctuations. The average period, L_p, is given from eq. 31,

$$L_p \simeq \frac{(\Delta V_{max} 4\pi\varepsilon\varepsilon_o)^2}{N} \tag{33}$$

Assigning the upper limit on the magnitude of potential fluctuations to be 0.5 eV, we calculated the period of the fluctuations, L_p, for each compensation level. From the period and the maximum magnitude of potential fluctuations, the average internal electric field, $\Delta V_{max}/L_p$, was obtained.

At low levels of compensation, the field arising from the potential fluctuations is small. The fluctuations are weak traps and the mobility is not strongly affected because the internal field is smaller than the externally applied field. At doping levels greater than 10^{-4}, the field due to potential fluctuations becomes dominant and exceeds the field applied during TOF by up to 2 orders of magnitude. As seen from Figure 22, this regime correlates with the region where the electron and hole mobilities converge.

The observed behavior of the optical absorption edge is understandable in terms of potential fluctuations. Optical absorption is a vertical transition in real space, as shown schematically in Fig. 25. Long range potential fluctuations therefore do not broaden the absorption because the local band gap is unchanged. Thus the absence of a doping dependence of the absorption edge at low doping levels in Fig. 24 is readily understood. The rapid increase in absorption slope at high doping levels is explained by an electric-field induced reduction of the gap through the Franz-Keldysh effect. The electric field arising from potential fluctuations tilts the band edges, as shown in Fig. 25. The average reduction in band gap is the product of the field due to potential fluctuations and the spatial extent of the electron wavefunction in amorphous silicon, R_o,

$$\Delta E_o \simeq \frac{R_o \Delta V_{max}}{L_p} = \frac{N R_o}{\Delta V_{max} (4\pi\varepsilon\varepsilon_o)^2} \tag{34}$$

The distribution of values of ΔE_o due to the random fluctuations leads us to associate ΔE_o with the broadening of the optical absorption edge. The shift is proportional to the doping concentration, and is only significant at the highest doping levels. R_o is taken to be on the order of 20 Å for states near the mobility edge. The change in absorption becomes significant compared to the absorption edge slope of undoped material ($\simeq$50 meV) at doping levels of 3×10^{-4} and greater. This corresponds to the level of compensation at which the large change in the absorption edge was observed. The sudden broadening of the optical absorption edge for compensation concentrations greater than 10^{-4} is consistent with a model of potential fluctuations in which sufficiently high fields allow tunneling transitions of lower energy to occur.

4. REMOTE HYDROGEN PLASMA (RHP) GROWTH

In the remote hydrogen plasma reactor the purpose of the plasma is to provide a flux of monatomic hydrogen for downstream reactions. The deposition of hydrogenated amorphous silicon (a-Si:H) involves the downstream injection of silane (SiH_4) to produce silyl radicals (SiH_3) as follows:

$$H + SiH_4 \xrightarrow{k_1} H_2 + SiH_3, \qquad (35)$$

where k_1 is the rate coefficient for the bimolecular reaction. Quantitative as well as qualitative characterization of such gas-phase reactions is essential to design deposition processes and for understanding the origin of film properties.

A. Plasma diagnostics using ESR

The kinetics of reactions such as Eq. 35 can be conveniently studied with electron spin resonance (ESR) since monatomic hydrogen is itself a radical and its consumption with time can be monitored with high sensitivity as a spatial variation of the H concentration. In the present study this approach has been applied to characterize the following reactant combinations that are of interest in the synthesis of amorphous materials: $H(D)+SiH_4$ and $H+C_2H_2$.

Two key measurement procedures are required to simplify the analysis of chemical-kinetic data from an ESR-flow system. First, the second-order (bimolecular) reaction law is reduced to pseudo-first order by adjusting the concentrations of the reactants so that $[H] \ll [SiH_4]$. Secondly, correction for the loss of H by processes that are first order in H and independent of SiH_4, such as wall recombination, is achieved by recording [H] at each position Δx downstream from the injector both with ("on")

and without ("off") flowing SiH_4; in the latter case the reactant was replaced by an equal flow of helium through the injector in order to keep the pressure (i.e., flow velocity v) unchanged. Then the rate coefficient k_1 is obtained from the expression

$$ln([H]|_{ON} / [H]|_{OFF}) = C_0 - k_1 [SiH_4] (\Delta x / v), \quad (36)$$

where C_0 is simply the ordinate for the arbitrarily chosen reference position $\Delta x = 0$.

Additional consumption of H by a fast secondary reaction, that involves a product of the primary reaction, can necessitate a correction for the stoichiometry of the net reaction in order to extract k_1 from the *observed* rate coefficient. For example, if every silyl radical is lost through the secondary reaction

$$H + SiH_3 \rightarrow SiH_4, \quad (37)$$

then the observed coefficient would be a factor of 2 larger than k_1. However, the stoichiometric correction is expected to be less than this since film deposition and disilane formation (e.g., $2SiH_3 \rightarrow Si_2H_6$) also contribute to silyl consumption.

Data on the decay of H or D with Δx for selected reactant pairs are shown in Fig. 26. Also listed are the observed rate coefficients obtained from the application of Eq. 36.

The primary reaction between H and C_2H_2 (acetylene) is expected to involve the addition of H to the unsaturated hydrocarbon, as occurs in the reaction of H and C_2H_4 (ethylene). In contrast, the reaction of H with the saturated hydrocarbon CH_4 (methane) involves hydrogen abstraction. With acetylene, as well as with ethylene, numerous secondary reactions are possible. This issue was investigated with conventional (quadrapole) mass spectrometry, which was available on a remote hydrogen plasma deposition reactor rather than on the ESR flow reactor. This experimental arrangement permitted detection of only chemically stable molecules (e.g., C_2H_2, C_2H_4, or C_2H_6 (ethane)) rather than radicals (e.g., C_2H_3 or C_2H_5) from the primary and secondary reactions.

The mass spectra in Fig. 27 were produced by mixing D and C_2H_2. It was estimated that at the injectors $[D] > [C_2H_2]$. The solid curve in Fig. 29(a) is primarily the cracking pattern for C_2H_2, and the dotted curve shows the change resulting from activation of the plasma. Only at high mass-anaylzer sensitivities could trace amounts of new molecules ascribable to (deuterated) ethylene and ethane be detected. The primary effect of mixing D and C_2H_2 was the production of C_2D_2. For example, the dominant peak of the solid curve in Fig. 27(a) appears at m/e

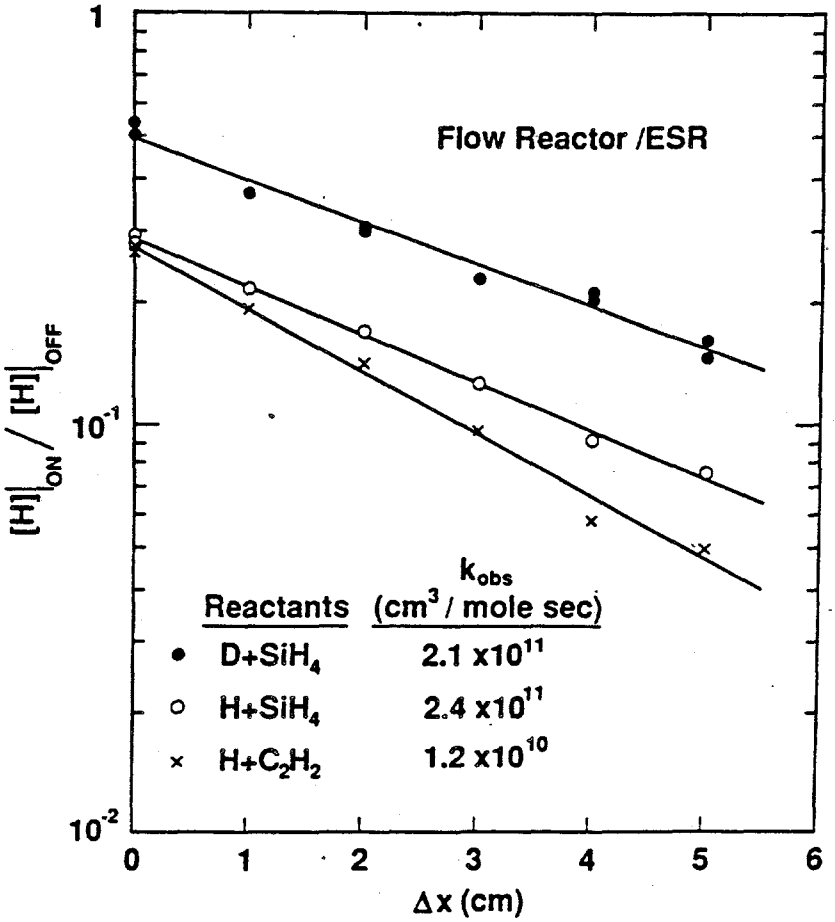

FIG.26. Variation of the H or D concentration with distance Δx down stream from the injector nozzle, for the injection of SiH_4 or C_2H_2.

(mass/charge) 26 and is due to $C_2H_2^+$. This peak shifts to *m/e* 28 with the plasma on, which reflects a nearly complete conversion to C_2D_2. Similarly, the *m/e*-13 peak (CH^+) shifts to *m/e* 14 (CD^+), while the peaks at *m/e* 12 and 24 remain unchanged since they arise from C^+ and C_2^+, respectively.

The mass spectra in Fig. 27 can be explained by the repeated occurrence of the following hydrogen addition and abstraction reactions:

$$D + C_2H_2 \rightarrow C_2H_2D \quad (38)$$

$$D + C_2H_2D \rightarrow C_2HD + DH \quad (39)$$

to produce C_2D_2.

The rate coefficients observed in this study are compared with previously published results in Table I; also listed are the experimental methods, the measurement pressures, and the coefficients for some related reactions. This study presents the first determination by the ESR flow reactor technique of the rate

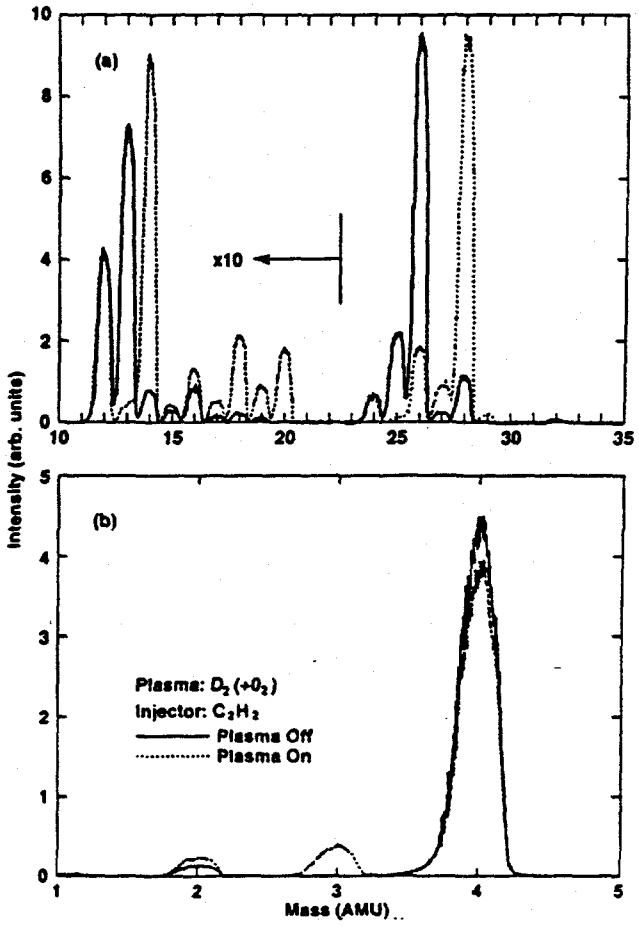

FIG. 27. Mass spectra for the reactions of D and C_2H_2 in a remote hydrogen plasma deposition reactor; (a) intermediate mass range and (b) low mass range. A small concentration of O_2 is added to suppress recombination.

coefficient for $H+SiH_4$. The previous values extend over a wide range (×20), and the present value agrees with those at the low end of this range. For $D+SiH_4$ the range of published coefficients is narrower (×6), and the present value falls within it. This may be the first experimental determination of the rate coefficient for $H+C_2H_2$. It is four orders of magnitude larger than that for $H+CH_4$, consequently acetylene may be a practical source gas for the deposition of carbon-containing films (e.g., a-SiC or diamond) in a remote hydrogen plasma reactor. Thus, the ESR/flow system method has proven to be a well-suited and informative technique to evaluate gas-phase reactions in such deposition systems.

TABLE 1: Rate coefficients for hydrogen-transfer reactions with selected group IV hydrides at room temperature, compared to previous measurements.

Reactants	Observed Rate Coefficient (cm^3 $mole^{-1}$ sec^{-1})	Other measurements (cm^3 $mole^{-1}$ sec^{-1})
$H + SiH_4$	2.4×10^{11} (2 Torr)	$2.6x10^{11}$ - $5.1x10^{12}$
$D + SiH_4$	2.1×10^{11} (2 Torr)	$9.0x10^{10}$ - $5.4x10^{11}$
$H+CH_4$	undetectable	(1.9×10^{6})*
$H+C_2H_2$	1.2×10^{10}	none
$H+C_2H_4$	not measured	2.0×10^{11} - $3.6x10^{11}$

B. NMR measurements of RHP films

NMR is a particularly effective tool to probe the resulting structure of hydrogen in a-Si:H and related materials. Here we report on H NMR data for films grown by the remote hydrogen plasma reactor and contrast the results with similar studies on films grown by glow discharge.

The room temperature hydrogen spectrum for the RHP a-Si:H sample is composed of two features, 40% of the signal consists of a narrow line (3 kHz FWHM), attributed to isolated Si-H units. The remaining 60% of the H signal resides in a broad line (26 kHz FWHM) identified as a clustered phase consisting of regions of high H concentration. These linewidths are constant within experimental error over the entire temperature range (4.2 - 300K). The linewidths and relative concentrations, as well as the overall H concentration of 9.7 atomic %, are very similar to what is found in high-quality GD deposited a-Si:H. However, differences in the NMR spectra become apparent as the temperature is lowered. Below 100K, a very narrow component (0.3 kHz FWHM) emerges from the noise as $< 5\%$ of the signal and slowly disappears as the temperature is lowered below 20K. This very narrow line is most likely due to motionally narrowed H species, similar to what has been reported in microcrystalline Si:H. Below 30K, a signal from non-bonded H_2 separates from the central resonance due to the orientational ordering of the molecules in the presence of electric field gradients. The ordering of the molecules

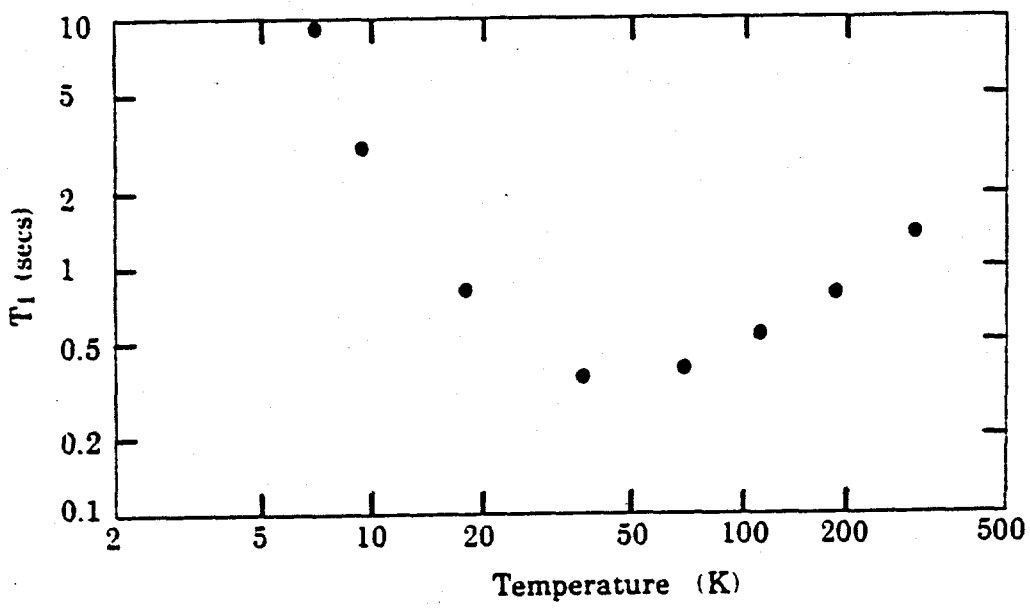

FIG. 28. Temperature dependence of the hydrogen spin-lattice relaxation time in an a-Si:H film deposited in a remote hydrogen plasma reactor.

appears as a 180 kHz split Pake doublet which comprises 10% of the total signal at 4.2K. Thus the RHP material contains much more molecular hydrogen than GD deposited films.

The spin-lattice relaxation time (T_1), shown in Figure 28, displays a minimum of 0.35 seconds at 50K, as in electronic grade GD deposited material. The T_1 minimum is due to the H_2 molecules which serve as relaxation centers for the bonded hydrogen. It is a measure of the number of molecules affecting the bulk hydrogen. In the case of good GD material, this has been shown to be a reliable a measure of the H_2 content in the films indicating that about half of the molecules affect the relaxation of the bulk hydrogen. However, in the present sample, fits to the T_1 data give a H_2 content of about 0.1 atomic %, an order of magnitude lower value than what is directly measured in the Pake doublet. Thus, it is likely that the molecules reside in large H_2 containing voids in which only the molecules at the internal surface interact strongly with the lattice and contribute to relaxation of bonded H.

A film deposited with a remote deuterium plasma (RDP) was measured and found to contain 1.1 atomic % deuterium which resides in both a narrow NMR line (0.9 kHz FWHM; 0.65 atomic %) and a broad line (20 kHz FWHM; 0.45 atomic %) at room temperature. The narrow line broadens to 3.6 kHz as the temperature is lowered to 1.6K and is indicative of a motionally narrowed species, the motion of

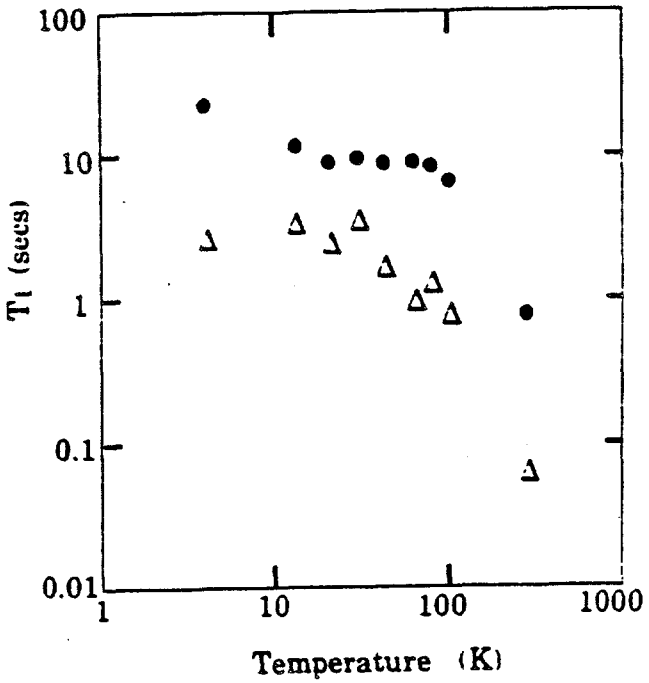

FIG. 29. Hydrogen spin-lattice relaxation time versus temperature for a deuterated remote plasma sample. The data are for the narrow line (points) and broad line (triangles).

which is constrained at the low temperature ranges. The relative amounts in the two lines remain constant over the entire temperature range, with spectral observation of molecular H_2, even at 1.6K.

The comparative absence of H_2 is reflected in the long spin lattice relaxation times for the narrow hydrogen signal over the temperature range (Figure 29). The two spectral components are seen to have different T_1's though both show the same increase in T_1 as the temperature is lowered from 290 to 80K. The narrow line exhibits a T_1 plateau of 9.5 seconds from 20 - 60K with no definable minimum. Hydrogen in the broad line relaxes much faster (0.08 seconds at 290K) than the narrow line and roughly parallels the narrow line as the temperature is lowered, but also exhibits no T_1 minimum. This is considered to be due to isolation of the bonded spins from relaxation centers. Very similar results have been reported for a GD deposited a-Ge:H sample in which an upper bound to the molecular hydrogen concentration was put at 0.0015 atomic %.

The deuterium NMR spectrum for the RDP sample consists of two components, a 66 kHz split doublet comprising 0.8 at. % deuterium, previously identified as arising from deuterium tightly bound to silicon atoms, and a narrow central line. The

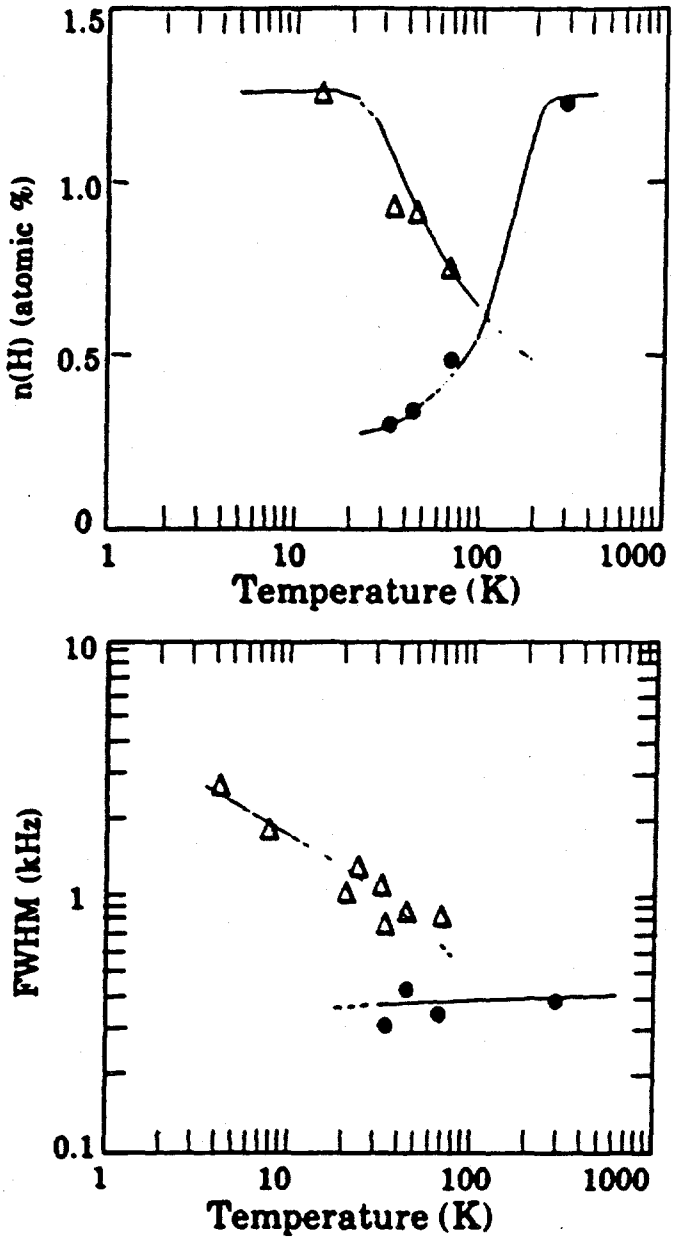

FIG. 30. Temperature dependence of the relative concentrations (uper curve) and linewidths (lower curve) for the central NMR deuterium lines. The data are for the narrow line (points) and broad line (triangles).

narrow central line (0.4 kHz FWHM; 1.24 atomic %) dominates the spectrum near room temperature and a somewhat broader line (0.8 - 2.5 kHz) dominates at lower temperatures (50 - 4.2K). The narrow line must be due to mobile deuterium. Figure 31 shows that at intermediate temperatures, there is a distribution of environments for the spins which causes a range of freeze-out temperatures rather that a continuous broadening of single species. This is analogous to the solidification transition of the H_2 molecules of the RHP sample and thus may be due to the

freezing out of HD translational motion similar to that of H_2. There is no direct spectral evidence of D_2 or HD as reported elsewhere for various GD deposited deuterated samples.

Publications list

Street, R.A. *The density of states distribution of bonded hydrogen in a-Si:H.* Solar Cells 30 (1991) 207-218.

Street, R.A. *Hydrogen chemical potential and structure of a-Si:H.* Physical Review B 43 (1991) 2454-2457.

Street, R.A. *Hydrogen diffusion and electronic metastability in amorphous silicon.* Physica B 170 (1991) 69-81.

Johnson, N. M.; Walker, J.; Stevens, K. S. *Characterization of a Remote Hydrogen Plasma Reactor with Electron Spin Resonance.* J. Appl. Phys., 69, 2631-2634 (1991).

Jackson, W. B.; Zhang, S. B., *Hydrogen complexes in amorphous silicon in Transport, Correlation and Structural Defects*, edited by H. Fritzsche series Advances in Disordered Semiconductors, (World Scientific, Singapore, 1990), pp. 63.

Zhang, S.B.; Jackson, W. B., *Formation of extended hydrogen complexes in silicon*, Phys. Rev. B 43 (1991), 12142.

Jackson; W. B.; Zhang, S. B., *Hydrogen complexes in hydrogenated silicon*, Physica B 170 (1991) 197.

Street, R. A. *Thermal generation currents in hydrogenated amorphous silicon p-i-n structures.* Applied Physics Letters. (1990) 57, 1334-1336.

Street, R. A. *Defect reactions, thermal equilibrium and metastability in a-Si:H.* Reviews of solid state science 2&3 (1990) 619-632.

Ready, S. E.; Boyce, J. B.; Johnson, N. M.; Walker, J.; Stevens, K. S. *Hydrogen Bonding in a-Si:H Prepared by Remote Hydrogen Plasma Deposition.* Amorphous Silicon Technology--1990 (Materials Research Society, Pittsburgh, PA, 1990), eds. P. C. Taylor, M. J. Thompson, P. G. LeComber, Y. Hamakawa, and A. Madan, Materials Research Society Symposium Proceedings Series, Vol. 192, pp. 127-132.

Street, R. A., *Long time transient conduction in a-Si:H p-i-n devices*, Philos. Mag. B63, (1991) 1343.

Howard, J. A., and Street, R. A., *Evidence for potential fluctuations in compensated amorphous silicon*, Phys Rev. B in press.

Santos, P. V., Jackson, W. B., And Street, R. A. *Saturation of light induced defects in a-Si:H*, AIP Conf. Proc., 234 51 (1991)

Document Control Page	1. SERI Report No. NREL/TP-214-4591	2. NTIS Accession No. DE92001177	3. Recipient's Accession No.

4. Title and Subtitle

Research on the Structural and Electronic Properties of Defects in Amorphous Silicon, Final Subcontract Report, September 1989 - December 1990

5. Publication Date
December 1991

6.

7. Author(s)
R.A. Street

8. Performing Organization Rept. No.

9. Performing Organization Name and Address

Xerox Palo Alto Research Center
Palo Alto, California 94304

10. Project/Task/Work Unit No.
PV141101

11. Contract (C) or Grant (G) No.

(C) HB-7-06056-1

(G)

12. Sponsoring Organization Name and Address
National Renewable Energy Laboratory
1617 Cole Blvd.
Golden, CO 80401-3393

13. Type of Report & Period Covered
Technical report,
September 1989 - December 1990

14.

15. Supplementary Notes
NREL technical monitor: B. Stafford, (303) 231-7126

16. Abstract (Limit: 200 words)

The work performed for this contract focused on the saturation of light-induced effects, hydrogen-mediated metastability and growth, defects and electronic properties, and remote hydrogen plasma growth. This work included research on hydrogen chemical reactions, hydrogen density-of-states model and metastability, hydrogen bonding configurations, a model for the role of hydrogen complexes in the metastability, and hydrogen chemical potential and growth structure. This document also covers research on thermal generation currents in p-i-n diodes, field dependence of the generation current, metastability effects at contacts, and potential fluctuations in compensated a-Si:H. Information is included on plasma diagnostics using electron spin resonance and nuclear magnetic resonance measurements of remote hydrogen plasma films.

17. Document Analysis
a. Descriptors
photovoltaics ; solar cells ; amorphous silicon ; density states ; defects

b. Identifiers/Open-Ended Terms

c. UC Categories
271

18. Availability Statement
National Technical Information Service
U.S. Department of Commerce
5285 Port Royal Road
Springfield, VA 22161

19. No. of Pages
58

20. Price
A04